



# TOI-1075 b: A Dense, Massive, Ultra-short-period Hot Super-Earth Straddling the Radius Gap

Zahra Essack<sup>1,2</sup>, Avi Shporer<sup>2</sup>, Jennifer A. Burt<sup>3</sup>, Sara Seager<sup>1,2,4</sup>, Saverio Cambioni<sup>1</sup>, Zifan Lin<sup>1</sup>, Karen A. Collins<sup>5</sup>, Eric E. Mamajek<sup>3</sup>, Keivan G. Stassun<sup>6,7</sup>, George R. Ricker<sup>2</sup>, Roland Vanderspek<sup>2</sup>, David W. Latham<sup>5</sup>, Joshua N. Winn<sup>8</sup>, Jon M. Jenkins<sup>9</sup>, R. Paul Butler<sup>10</sup>, David Charbonneau<sup>5</sup>, Kevin I. Collins<sup>11</sup>, Jeffrey D. Crane<sup>12</sup>, Tianjun Gan<sup>13</sup>, Coel Hellier<sup>14</sup>, Steve B. Howell<sup>9</sup>, Jonathan Irwin<sup>15</sup>, Andrew W. Mann<sup>16</sup>, Ali Ramadhan<sup>1</sup>, Stephen A. Shectman<sup>12</sup>, Johanna K. Teske<sup>10</sup>, Samuel W. Yee<sup>8</sup>, Ismael Mireles<sup>17</sup>, Elisa V. Quintana<sup>18</sup>, Peter Tenenbaum<sup>9,19</sup>, Guillermo Torres<sup>5</sup>, and Elise Furlan<sup>20</sup>

<sup>1</sup> Department of Earth, Atmospheric and Planetary Sciences, Massachusetts Institute of Technology, Cambridge, MA 02139, USA; [zessack@mit.edu](mailto:zessack@mit.edu)

<sup>2</sup> Department of Physics and Kavli Institute for Astrophysics and Space Research, Massachusetts Institute of Technology, Cambridge, MA 02139, USA

<sup>3</sup> Jet Propulsion Laboratory, California Institute of Technology, 4800 Oak Grove Drive, Pasadena, CA 91109, USA

<sup>4</sup> Department of Aeronautics and Astronautics, MIT, 77 Massachusetts Avenue, Cambridge, MA 02139, USA

<sup>5</sup> Center for Astrophysics, Harvard & Smithsonian, 60 Garden Street, Cambridge, MA 02138, USA

<sup>6</sup> Department of Physics and Astronomy, Vanderbilt University, Nashville, TN 37235, USA

<sup>7</sup> Department of Physics, Fisk University, Nashville, TN 37208, USA

<sup>8</sup> Department of Astrophysical Sciences, Princeton University, 4 Ivy Lane, Princeton, NJ 08544, USA

<sup>9</sup> NASA Ames Research Center, Moffett Field, CA 94035, USA

<sup>10</sup> Earth & Planets Laboratory, Carnegie Institution for Science, 5241 Broad Branch Road, NW, Washington, DC 20015, USA

<sup>11</sup> George Mason University, 4400 University Drive, Fairfax, VA 22030, USA

<sup>12</sup> The Observatories of the Carnegie Institution for Science, 813 Santa Barbara Street, Pasadena, CA 91101, USA

<sup>13</sup> Department of Astronomy, Tsinghua University, Beijing 100084, People's Republic of China

<sup>14</sup> Astrophysics Group, Keele University, Staffordshire, ST5 5BG, UK

<sup>15</sup> Institute of Astronomy, University of Cambridge, Madingley Road, Cambridge, CB3 0HA, UK

<sup>16</sup> Department of Physics and Astronomy, The University of North Carolina at Chapel Hill, Chapel Hill, NC 27599-3255, USA

<sup>17</sup> Department of Physics and Astronomy, University of New Mexico, 210 Yale Boulevard NE, Albuquerque, NM 87106, USA

<sup>18</sup> NASA Goddard Space Flight Center, 8800 Greenbelt Road, Greenbelt, MD 20771, USA

<sup>19</sup> SETI Institute, Mountain View, CA 94043, USA

<sup>20</sup> NASA Exoplanet Science Institute, Caltech/IPAC, Mail Code 100-22, 1200 East California Boulevard, Pasadena, CA 91125, USA

Received 2022 July 13; revised 2022 October 12; accepted 2022 October 19; published 2023 January 10

## Abstract

Populating the exoplanet mass–radius diagram in order to identify the underlying relationship that governs planet composition is driving an interdisciplinary effort within the exoplanet community. The discovery of hot super-Earths—a high-temperature, short-period subset of the super-Earth planet population—has presented many unresolved questions concerning the formation, evolution, and composition of rocky planets. We report the discovery of a transiting, ultra-short-period hot super-Earth orbiting TOI-1075 (TIC 351601843), a nearby ( $d = 61.4$  pc) late-K/early-M-dwarf star, using data from the Transiting Exoplanet Survey Satellite. The newly discovered planet has a radius of  $1.791^{+0.116}_{-0.081} R_{\oplus}$  and an orbital period of 0.605 day (14.5 hr). We precisely measure the planet mass to be  $9.95^{+1.36}_{-1.30} M_{\oplus}$  using radial velocity measurements obtained with the Planet Finder Spectrograph mounted on the Magellan II telescope. Our radial velocity data also show a long-term trend, suggesting an additional planet in the system. While TOI-1075 b is expected to have a substantial H/He atmosphere given its size relative to the radius gap, its high density ( $9.32^{+2.05}_{-1.85} \text{ g cm}^{-3}$ ) is likely inconsistent with this possibility. We explore TOI-1075 b's location relative to the M-dwarf radius valley, evaluate the planet's prospects for atmospheric characterization, and discuss potential planet formation mechanisms. Studying the TOI-1075 system in the broader context of ultra-short-period planetary systems is necessary for testing planet formation and evolution theories and density-enhancing mechanisms and for future atmospheric and surface characterization studies via emission spectroscopy with the JWST.

*Unified Astronomy Thesaurus concepts:* Exoplanets (498); Extrasolar rocky planets (511); Super Earths (1655); Radial velocity (1332); Transit photometry (1709); Planetary system formation (1257)

## 1. Introduction

Hot super-Earths are a subset of the super-Earth planet population ( $1 R_{\oplus} < R_p < 2 R_{\oplus}$ ) with short orbital periods ( $P < 10$  days) and surface temperatures high enough to melt silicate rock ( $T > 800$  K) due to strong irradiation by their host

stars. Hot super-Earths are compelling objects to study for the insights that they provide into atmospheric loss/retention, volatile cycling, the behaviors of materials at extreme temperatures, and Earth's early history as a magma-ocean planet.

NASA's Kepler space telescope (Borucki et al. 2010) transformed our understanding of exoplanets with discoveries of new planet classes and planetary systems. One of the Kepler mission's most revolutionary scientific results was that among the short-period planets it was sensitive to ( $P < 100$  days), the

size of the most common planet in the galaxy is between the size of Earth and Neptune ( $1-4 R_{\oplus}$ ), which has no solar system analog (Batalha 2014). This population of planets is subdivided into super-Earths,  $1 R_{\oplus} < R_p < 2 R_{\oplus}$ , and sub-Neptunes,  $2 R_{\oplus} < R_p < 4 R_{\oplus}$  (Fulton et al. 2017). The repurposing of the Kepler mission into K2 (Howell et al. 2014) provided the opportunity to search for many more ultra-short-period (USP) planets ( $P < 1$  day). The K2 campaigns observed target fields in the ecliptic plane for 80 days at a time, making USP planets easily detectable within this observing window (Adams et al. 2016, 2017, 2021; Malavolta et al. 2018).

There are many unresolved theories regarding the atmospheres of hot super-Earths, including whether they exist (e.g., Kreidberg et al. 2019), what they are composed of (e.g., Schaefer & Fegley 2009; Ito et al. 2015; Mansfield et al. 2019), and how they evolve. The “radius gap”—a local minimum in the planet radius distribution at  $1.75 R_{\oplus}$  for planets orbiting Sun-like stars and with  $P < 100$  days (Fulton et al. 2017)—is theorized to separate predominantly rocky planets from planets with a substantial H/He atmosphere (Owen & Wu 2017). The location of the radius gap is dependent on the host star type and shifts to a smaller radius as the stellar radius decreases, as seen for planets around M dwarfs (Zeng et al. 2017; Cloutier & Menou 2020). Rogers (2015) found that, statistically, planets with  $R_p > 1.6 R_{\oplus}$  have a volatile-rich envelope. A variety of compositions have been determined for rocky planets below the radius gap, including Earth-like compositions (e.g., Pepe et al. 2013; Dressing et al. 2015) and high-density compositions akin to Mercury (e.g., Santerne et al. 2018; Lam et al. 2021; Silva et al. 2022).

To explain the existence of the radius gap/valley, multiple theoretical models have been suggested. These include photoevaporation (atmospheric loss driven by stellar irradiation; Lopez et al. 2012; Chen & Rogers 2016; Owen & Wu 2017), core-powered mass loss (atmospheric loss driven by the cooling of the planetary core after formation, resulting in the escape of the outer layers of the atmosphere; Ginzburg et al. 2018; Gupta & Schlichting 2019, 2020), and gas-poor formation (the formation of distinct rocky and nonrocky planet populations, where the rocky planet population is a result of delayed gas accretion within the protoplanetary disk until a point where the gas in the disk has almost fully dissipated; Lee et al. 2014; Lee & Chiang 2016; Lopez & Rice 2018; Cloutier & Menou 2020).

While planets discovered by Kepler have well-constrained radii measurements, the vast majority lack corresponding mass measurements because the planets orbit faint stars, making detailed follow-up investigations difficult. NASA’s Transiting Exoplanet Survey Satellite (TESS; Ricker et al. 2014) mission, the successor of Kepler, is an all-sky survey of bright, nearby stars with a minimum observing baseline of  $\sim 27$  days. TESS has identified hundreds of short-period super-Earth planet candidates amenable to follow-up observations with radial velocity (RV) instruments to determine their masses since it began operations in 2018 (Guerrero et al. 2021). Here we present the discovery and confirmation of TOI-1075 b, a USP super-Earth around TOI-1075 ( $V = 12.75$  mag) monitored by TESS with a planetary radius located slightly above the radius gap. Obtaining precise radii and masses for the small, close-in TESS planet candidates that span the radius valley is crucial for elucidating the atmospheric composition and evolution of hot super-Earths via further spectroscopic characterization and for

**Table 1**  
Astrometry and Photometry for TOI-1075

Parameter	Value	Source
Designations	TIC 351601843	Stassun et al. (2019)
R.A. (ICRS, J2000)	20:39:53.082	Gaia DR3
Decl. (ICRS, J2000)	−65:26:58.95	Gaia DR3
$\mu$ R.A. (mas yr <sup>−1</sup> )	−99.8399 ± 0.0081	Gaia DR3
$\mu$ decl. (mas yr <sup>−1</sup> )	−60.016 ± 0.013	Gaia DR3
Parallax (mas)	16.2816 ± 0.0132	Gaia DR3
Distance (pc)	61.43 <sup>+0.18</sup> <sub>−0.67</sub>	Gaia DR3
$v_R$ (km s <sup>−1</sup> )	31.07 ± 0.30	Gaia DR3
Spectral type	K9V/M0V	Pecaut & Mamajek (2013)
$B$ (mag)	14.108 ± 0.028	APASS/DR10
$V$ (mag)	12.751 ± 0.077	APASS/DR10
$g'$ (mag)	13.423 ± 0.027	APASS/DR10
$r'$ (mag)	12.181 ± 0.088	APASS/DR10
$i'$ (mag)	11.504 ± 0.143	APASS/DR10
TESS (mag)	10.2565 ± 0.0074	TICv8
$G$ (mag)	12.0447 ± 0.0028	Gaia DR3
$G_{BP}$ (mag)	12.9442 ± 0.0028	Gaia DR3
$G_{RP}$ (mag)	11.1069 ± 0.0038	Gaia DR3
$J$ (mag)	9.935 ± 0.023	2MASS
$H$ (mag)	9.292 ± 0.026	2MASS
$K_s$ (mag)	9.115 ± 0.023	2MASS
$W_1$ (mag)	9.001 ± 0.025	WISE
$W_2$ (mag)	9.001 ± 0.021	WISE
$W_3$ (mag)	8.915 ± 0.024	WISE
$W_4$ (mag)	8.806 ± 0.315	WISE

furthering our understanding of planetary compositions by studying planetary system architectures and formation histories.

This paper is structured as follows. In Section 2, we describe the properties of the host star, TOI-1075. In Section 3, we describe the time-series photometry and RV data sets we obtained for the TOI-1075 system. In Section 4, we describe our data analysis, including a global model fit, and derive properties for the planetary system. In Section 5, we discuss the new star–planet system, including atmospheric characterization prospects and a review of potential formation mechanisms for TOI-1075 b, and finally, we provide our conclusions in Section 6.

## 2. Stellar Data and Characterization

### 2.1. Astrometry and Photometry

Stellar astrometry and visible and infrared photometry for TOI-1075 (TIC 351601843, 2MASS J20395334−6526579, APASS 31990797, Gaia DR3 6426188308031756288, UCAC 4123-179251) are compiled in Table 1. The positions, proper motions, parallax, RV, and Gaia photometry are from Gaia DR3 (Prusti et al. 2016; Gaia Collaboration et al. 2022, in preparation). We convert the astrometry to Galactic velocities following ESA (1997).<sup>21</sup> Photometry is reported from APASS Data Release 10 (Henden et al. 2016),<sup>22</sup> the TESS Input Catalog (TICv8; Stassun et al. 2019), the Two Micron All Sky Survey (2MASS; Cutri et al. 2003), and the Wide-field Infrared Survey Explorer (WISE; Cutri et al. 2012). From comparison

<sup>21</sup>  $U$  toward the Galactic center,  $V$  in the direction of Galactic spin, and  $W$  toward the north Galactic pole (ESA 1997).

<sup>22</sup> <https://www.aavso.org/apass>

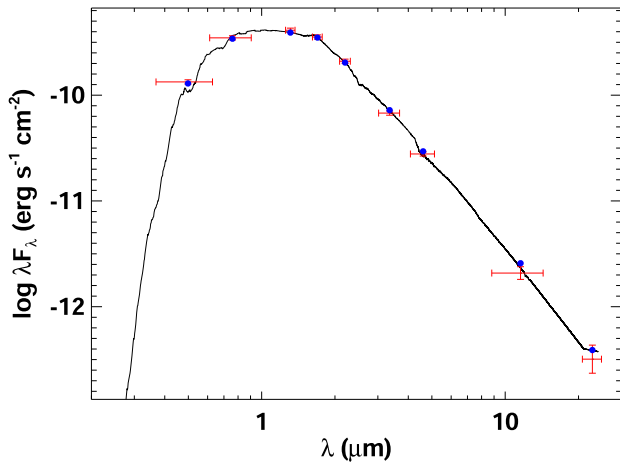


**Figure 1.** The SED of TOI-1075. Red symbols represent the observed photometric measurements, where the horizontal bars represent the effective width of the passband. Blue symbols are the model fluxes from the best-fit NextGen atmosphere model (black).

of the star’s colors ( $B - V = 1.42$ ,  $V - K_s = 3.58$ ,  $G - K_s = 2.93$ ,  $V - J = 2.76$ ,  $G_{BP} - G_{RP} = 1.84$ ) and absolute magnitude ( $M_V = 8.76$ ,  $M_G = 8.10$ ,  $M_{K_s} = 5.17$ ) with typical parameters for stars of various spectral types, TOI-1075’s photometry appears to be consistent with that of a typical main-sequence star intermediate between K9V and M0V types (Pecaut & Mamajek 2013).

## 2.2. Spectral Energy Distribution

As an independent determination of the basic stellar parameters, we performed an analysis of the broadband spectral energy distribution (SED) of the star, together with the Gaia DR3 parallax (with no systematic offset applied; see, e.g., Stassun & Torres 2021), in order to determine an empirical measurement of the stellar radius and mass following the procedures described in Stassun & Torres (2016) and Stassun et al. (2017, 2018). We pulled the  $JHK_s$  magnitudes from 2MASS, the  $W1$ – $W4$  magnitudes from WISE, and the  $G$ ,  $G_{BP}$ , and  $G_{RP}$  magnitudes from Gaia. Together, the available photometry spans the stellar SED over the wavelength range 0.4–20  $\mu\text{m}$  (see Figure 1).

We performed a fit using NExtGen stellar atmosphere models, with the free parameters being the effective temperature ( $T_{\text{eff}}$ ) and metallicity ( $[\text{Fe}/\text{H}]$ ). The remaining free parameter is the extinction  $A_V$ , which we fixed at zero due to the star’s proximity.<sup>23</sup> The resulting fit (Figure 1) has a reduced  $\chi^2$  of 1.4, with a best-fit  $T_{\text{eff}} = 3875 \pm 75$  K and  $[\text{Fe}/\text{H}] = -0.5 \pm 0.5$ . Integrating the model SED gives the observed bolometric flux,  $F_{\text{bol}} = 5.82 \pm 0.14 \times 10^{-10}$   $\text{erg s}^{-1} \text{cm}^{-2}$  ( $m_{\text{bol}} = 11.590 \pm 0.026$  mag on the IAU 2015 scale). Adopting the Gaia DR3 parallax ( $\varpi = 16.2816 \pm 0.0132$  mas), this leads to a bolometric luminosity of  $\log(L_{\text{bol}}/L_{\odot}) = -1.163 \pm 0.010$ . Combining the luminosity with the derived  $T_{\text{eff}}$  provides an estimate of the stellar radius of  $R_{\star} = 0.581 \pm 0.024 R_{\odot}$ . In addition, we can estimate the stellar mass from the empirical  $M_K$ -based relations of Mann et al. (2019), which give  $M_{\star} = 0.604 \pm 0.030 M_{\odot}$ . Moreover, the radius and mass together imply a mean stellar density of  $\rho_{\star} = 4.34 \pm 0.57 \text{ g cm}^{-3}$ .

<sup>23</sup> The STILISM 3D reddening maps from Lallement et al. (2018) estimate the reddening toward TOI-1075 to be  $E(B - V) = 0.004 \pm 0.016$ , i.e., negligible.

## 2.3. Stellar Mass and Radius from Empirical Relations

While we adopt the host star parameters derived above (Section 2.2) based on the SED and NExtGen models, we estimated those parameters using the empirical relations of Mann et al. (2019) and Boyajian et al. (2012), for comparison. We used the Gaia DR3 distance to derive the absolute  $K$ -band magnitude from the observed 2MASS magnitude, resulting in  $M_K = 5.173 \pm 0.023$  mag.

Next, we used the empirical relation between stellar mass and  $M_K$  provided by Mann et al. (2019; see their Table 6 and Equation (2)). Assuming a conservative uncertainty of 5%, this resulted in  $M_{\star} = 0.571 \pm 0.029 M_{\odot}$ . We note that the empirical relations provided by Mann et al. (2019) cover a mass range that reaches about  $0.75 M_{\odot}$  and a  $K$ -band magnitude up to about 4 mag, so the TOI-1075 host star is well within that range. For comparison, we calculated the stellar mass with the empirical relation of Mann et al. (2015; see their Table 1 and Equation (10)), resulting in  $0.604 \pm 0.030 M_{\odot}$ , which is 5% from the above estimate.

To estimate the stellar radius, we used the mass derived above and the radius–mass empirical relation derived by Boyajian et al. (2012; their Equation (10)), resulting in  $0.541 \pm 0.027 R_{\odot}$ . For comparison, using the empirical relation between radius and  $M_K$  of Mann et al. (2015; see their Table 1) results in  $R_{\star} = 0.580 \pm 0.029 R_{\odot}$ , which is 7% or  $1.3\sigma$  larger than the above estimate.

For the subsequent analyses in this paper, we adopt the stellar parameters derived from the SED analysis following Stassun & Torres (2016) and Stassun et al. (2017, 2018), namely,  $R_{\star} = 0.581 \pm 0.024 R_{\odot}$ ,  $M_{\star} = 0.604 \pm 0.030 M_{\odot}$ , and  $T_{\text{eff}} = 3875 \pm 75$  K.

## 2.4. Speckle Observations

If a star hosting a planet candidate has a closely bound stellar companion (or companions), the companion can create a false-positive exoplanet detection if it is a stellar eclipsing binary. Additionally, flux from these companion source(s) can lead to an underestimated planetary radius if not accounted for in the transit model (Ciardi et al. 2015). To search for close-in bound companions unresolved in our other follow-up observations, we obtained high-resolution speckle imaging observations.

TOI-1075 was observed on 2019 September 12 UT using the Zorro speckle instrument on Gemini-South (Scott et al. 2021). Zorro provides simultaneous speckle imaging in two bands ( $562 \pm 54$  and  $832 \pm 40$  nm) with output data products including a reconstructed image and robust contrast limits on companion detections (Howell et al. 2011, 2016). Figure 2 shows the  $5\sigma$  limiting contrast curves for the Zorro observations in both 562 (blue line) and 832 (red line) nm and the 832 nm reconstructed speckle image. We find that TOI-1075 is a single star with no companion brighter than  $\delta m = 5$ –6 mag at 832 nm from about  $0''.1$  out to  $1''.2$ . At the distance to TOI-1075 ( $d = 61.4$  pc), these angular limits correspond to spatial separations of 6–74 au.

## 2.5. Stellar Kinematics and Population

Gaia Collaboration et al. (2022, in preparation) provided the most accurate position and proper motion for TOI-1075 (= Gaia DR3 6426188308031756288), and Bailer-Jones et al. (2021) converted the Gaia DR3 trigonometric parallax ( $\varpi = 16.282 \pm 0.013$  mas) into a geometric distance of

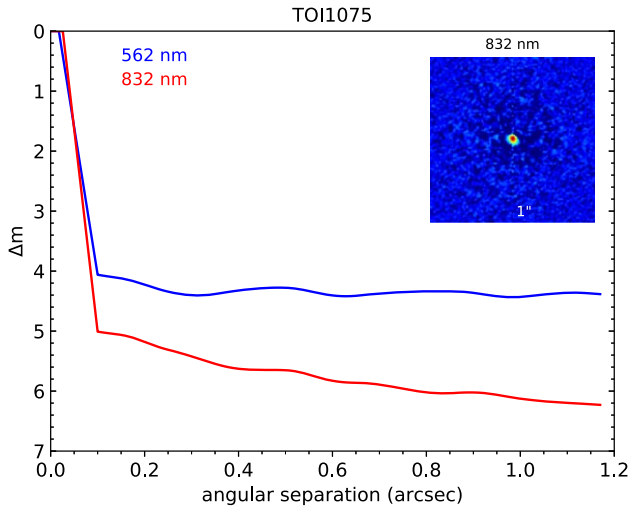


**Figure 2.** Gemini-South Zorro contrast curves for 562 (blue line) and 832 (red line) nm speckle observations and 832 nm image (inset) of TOI-1075. No visual companions are detected anywhere in Zorro’s field of view.

$d = 61.43_{-0.67}^{+0.18}$  pc. Gaia Collaboration et al. (2018) listed a median RV of  $v_r = 31.07 \pm 0.30$  km s<sup>-1</sup> averaged over 24 epochs. Using formulae from ESA (1997), we convert the Gaia DR3 astrometry and RV into Galactic barycentric velocities:  $U, V, W = 33.49, -31.58, 7.49 (\pm 0.22, 0.30, 0.20)$  km s<sup>-1</sup>.<sup>24</sup> The star’s 3D velocity is not near any of the 29 nearby young stellar groups tracked by Gagné et al. (2018), and the BANYAN  $\Sigma$  tool<sup>25</sup> returns membership probabilities of zero (<0.1%). Using the formulae and parameters from Bensby et al. (2014), we estimate Galactic population kinematic membership probabilities for TOI-1075 of  $P(\text{thin disk}) = 98.2\%$ ,  $P(\text{thick disk}) = 1.8\%$ ,  $P(\text{halo}) = 4.2 \times 10^{-3}\%$ , and  $P(\text{Hercules}) = 1.3 \times 10^{-2}\%$ ; i.e., TOI-1075 is  $\sim 56\times$  more likely to be a thin disk star than a thick disk star based on its velocity alone. The oldest thin disk stars are approximately  $\sim 8\text{--}9$  Gyr (e.g., Fuhrmann et al. 2017; Kilic et al. 2017; Fantin et al. 2019; Tononi et al. 2019).

We calculated the 3D separation between TOI-1075 and all of the stars in the Gaia Catalogue of Nearby Stars (GCNS; Gaia Collaboration et al. 2021) to search for any potential stellar companions. We find that TOI-1075 has no neighbors within 2 pc, and Gaia DR3 6429596764016919296 ( $\Delta = 2.00$  pc; component of the tight binary 2MASS 20335172–6403200) is its nearest star.

The systematic survey for common proper-motion companions to stars within 100 pc by Kervella et al. (2022) did not yield any matches of TOI-1075 with any Hipparcos stars. A query of the Gaia Collaboration et al. (2022, in preparation) catalog within  $2^\circ$  ( $\sim 2.0$  pc) of TOI-1075 searching among stars with parallaxes and proper motions within 25% of the values for TOI-1075 yielded no plausible common proper-motion companions. Thus, TOI-1075 appears to be a single star.

The space velocity of TOI-1075 may provide some additional clues about its age. In the GCNS catalog of stars within 100 pc, there are 153 stars whose  $UVW$  velocities are within 10 km s<sup>-1</sup> of TOI-1075. Thirty-eight of the 153 stars are lacking SIMBAD entries and have not been noted in the

literature. Among the 115 with SIMBAD entries, 60 have fiducial spectral types in SIMBAD, and none are hotter than the F5V star HD 43879 ( $T_{\text{eff}} = 6566 \pm 86$  K; Casagrande et al. 2011). A query of stellar parameter catalogs with mass estimates (Schofield et al. 2019; Stassun et al. 2019; Paegert et al. 2021; Reiners et al. 2022) shows that among the  $d < 100$  pc stars with velocities within 10 km s<sup>-1</sup> of TOI-1075, there is a noticeable lack of stars more massive than  $1.40 M_\odot$ .<sup>26</sup> The list of GCNS stars with velocities within 10 km s<sup>-1</sup> of TOI-1075 was also queried through the compendium of chromospheric activity measurements ( $\log R'_{\text{HK}}$ ) from Boro Saikia et al. (2018). Only eight of the stars had  $\log R'_{\text{HK}}$  measurements, and only two had  $\log R'_{\text{HK}} > -4.8$  (approximately corresponding to the Sun on its very most active days; Egeland et al. 2017): the planet host star HD 128356 (HIP 71481; K2.5IV,  $\log R'_{\text{HK}} = -4.73$ ) and 6 And (HD 218804, HIP 114430; F5V,  $\log R'_{\text{HK}} = -4.52$ ). The latter is a  $2.99_{-0.99}^{+0.48}$  Gyr old, fast-rotating ( $v \sin i = 19$  km s<sup>-1</sup>; Schröder et al. 2009) F5V star near the Kraft break, so not unusually fast-rotating or young. The  $\log R'_{\text{HK}}$  value for HD 128356 ( $-4.73$ ) appears to be spurious, however, as the assumed  $B - V$  color from Hipparcos (0.685) is based on a single ground-based measurement (Mermilliod et al. 1997), which is at odds with the star’s spectral type (K3V or K2.5IV; Uppgren et al. 1972; Gray et al. 2006) and  $T_{\text{eff}}$ , for which the published estimates are in tight agreement (4932–4953 K; Luck 2018; Soto & Jenkins 2018; Sousa et al. 2018). Adopting the  $B - V$  estimate for HD 128356 from the Tycho catalog ( $1.04 \pm 0.02$  mag), which is more consistent with that for a K3 dwarf star, the median Mt. Wilson  $S$ -value quoted by Boro Saikia et al. (2018;  $S = 0.214$ ) translates (via formulae from Noyes et al. 1984) to a more benign chromospheric activity level of  $\log R'_{\text{HK}} = -5.06$ . Hence, the stars that have 3D velocities within 10 km s<sup>-1</sup> of TOI-1075 that are Sun-like (excluding the mid-F star 6 And) with Ca H and K indices all have  $\log R'_{\text{HK}} < -4.8$ , consistent with ages of  $\gtrsim 3$  Gyr (Mamajek & Hillenbrand 2008).

We conclude that the lack of  $>1.40 M_\odot$  stars with similar velocities to TOI-1075 suggests that stars with similar orbits are unlikely to be  $\lesssim 2$  Gyr, and the small number of stars with published chromospheric activity indices seem to tell a similar story (lacking in stars  $\lesssim 3$  Gyr). It appears that stars younger than  $\lesssim 2$  Gyr have not yet scattered into the velocity space adjacent to the orbit of TOI-1075, suggesting that the star is either a middle-aged or old thin disk star, likely with an age between 2 and 9 Gyr.

## 2.6. Metallicity

TOI-1075 was spectrally characterized by the RAVE (RAVE J203953.3–652658; Kordopatis et al. 2013; Kunder et al. 2017; Steinmetz et al. 2020) and GALAH (Buder et al. 2018, 2021) stellar spectroscopy surveys, from which wildly disparate metallicity estimates have been published, ranging from  $[M/H] = -0.99 \pm 0.09$  (Kunder et al. 2017) to  $[Fe/H] = 0.38 \pm 0.07$  (Buder et al. 2021).

An independent photometric estimate of the metallicity can be made based on the star’s position on a color–magnitude

<sup>24</sup> The velocities are within 0.01 km s<sup>-1</sup> of that reported in the Gaia GCNS catalog (Gaia Collaboration et al. 2021).

<sup>25</sup> <http://www.exoplanetes.umontreal.ca/banyan/banyansigma.php>

<sup>26</sup> HIP 29888 (HD 43879;  $1.38 \pm 0.23 M_\odot$ ) in TICv8.2 (Paegert et al. 2021) and HIP 29888, HIP 111971 (HD 214729), and HIP 70196 (HD 125346) in Reiners & Zechmeister (2020)—all with mass estimates of  $1.40 M_\odot$ —defining the upper mass envelope.

diagram. Using the  $V - K_s$  versus  $M_{K_s}$  calibration from Johnson & Apps (2009) and Schlafman & Laughlin (2010), we find that the color–magnitude position for TOI-1075 ( $V - K_s = 3.584$ ,  $M_{K_s} = 5.176$ ) is only 0.056 mag below the mean main sequence for late-K and M dwarfs, translating to photometric metallicity estimates of  $[\text{Fe}/\text{H}] = -0.08$  (Johnson & Apps 2009) and  $-0.21$  (Schlafman & Laughlin 2010). A similar estimate can be done using 2MASS and Gaia photometry by interpolating the photometry and metallicities of nearby M dwarfs in Mann et al. (2015). As with  $V - K_s$  versus  $M_{K_s}$ , the star sits slightly below the solar-metallicity sequence in  $M_G$  using  $B_P - R_P$ ,  $J - K$ , or  $G - K_s$ . This interpolation method gave us a metallicity estimate of  $[\text{Fe}/\text{H}] = -0.10 \pm 0.12$ , consistent with the first estimate from Johnson & Apps (2009).

We also analyzed the iodine-free Planet Finder Spectrograph (PFS) template spectrum using the publicly available code SpecMatch-Emp (Yee et al. 2017). This code matches a target spectrum with a library of observed spectra from stars with empirically determined stellar properties and is particularly well suited for the analysis of late-type stars. We recovered  $T_{\text{eff}} = 3824 \pm 70$  K,  $R_* = 0.57 \pm 0.06 R_{\odot}$ , and  $[\text{Fe}/\text{H}] = -0.08 \pm 0.09$  dex. The SpecMatch-Emp recovered metallicity thus corroborates the photometric metallicity measurement.

### 2.7. Stellar Variability

WASP-South, an array of eight cameras composed of Canon 200 mm,  $f/1.8$  lenses backed by  $2k \times 2k$  CCDs, was the southern station of the WASP transit-search survey (Pollacco et al. 2006). The field of TOI-1075 was observed every year from 2008 to 2012, covering spans of 100–180 days in each year. Within each night, the cadence was typically 15 minutes, accumulating a total of 38,000 data points. TOI-1075 is the only bright star in the  $48''$  photometric extraction aperture. We searched the WASP data for a rotational modulation using the methods described in Maxted et al. (2011), but we found no significant modulation for any period between 1 and 100 days. Within each season, the 95% confidence upper limit on the amplitude is 3 mmag. Combining all of the years of data results in an upper limit of 1.6 mmag. The periodograms of each season of WASP-South data showing no significant rotation modulation are shown in Figure 3. The peaks near 30 days are compatible with the residual effects of moonlight propagating through the pipeline at a low level and thus are unlikely to be caused by TOI-1075. The lack of any rotational modulation is unusual for a cool star. McQuillan et al. (2014) reported that 83% of stars cooler than 4000 K in the Kepler field show a rotational modulation, with most having amplitudes in the range 3–10 mmag. Hence, TOI-1075 is among the least photometrically variable  $\sim 20\%$  of stars of its spectral type. Its low levels of stellar variability support the finding that the star is at least 2 Gyr old.

## 3. Exoplanet Detection and Follow-up

### 3.1. TESS Time-series Photometry

The TESS primary mission surveyed the northern and southern ecliptic hemispheres in sectors measuring  $24^\circ \times 96^\circ$ , with near-continuous photometric coverage over  $\sim 27$  days. The TESS Primary Mission ran for 2 years (2018 July–2020 July) and consisted of 26 sectors. TESS began its first extended

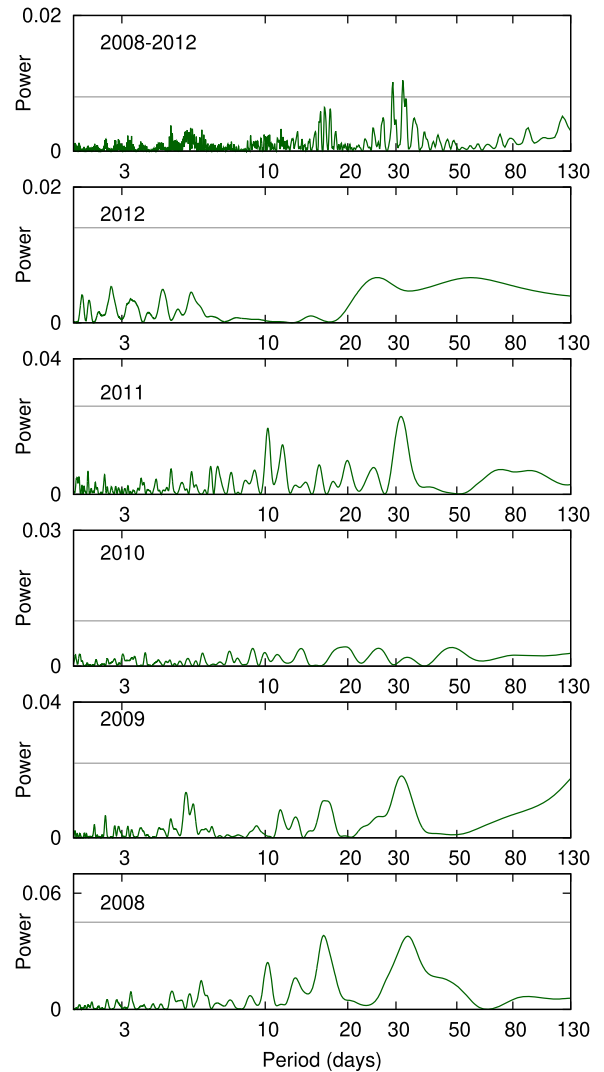


**Figure 3.** Periodograms of each season of WASP data for TOI-1075, showing the absence of any significant rotational modulation. The horizontal lines mark the 95% confidence false-alarm level. The top panel is the periodogram for the 5 yr of data combined.

mission in 2020 July, which will end in 2022 September (when the second extended mission is scheduled to commence) and consists of 29 sectors. TOI-1075 (TIC 351601843, 2MASS J20395334–6526579) was selected for transit detection observations by TESS with 2 minutes cadence as part of the Candidate Target List, a preselected target list prioritized for the detection of small planets (Stassun et al. 2018, 2019). TOI-1075 was observed by TESS in Sector 13 from UT 2019 June 19 through 2019 July 18 during the primary mission and again from UT 2020 July 4 through 2020 July 30 in Sector 27 during the first TESS Extended Mission. The star fell on Camera 2 in both sectors.

The raw TESS data for TOI-1075 were processed with the Science Processing Operations Center Pipeline (SPOC; Jenkins et al. 2016), which performs pixel calibration, light-curve extraction, deblending from nearby stars, and removal of common-mode systematic errors, and are available at the Mikulski Archive for Space Telescopes (MAST) website.<sup>27</sup> The SPOC data include both simple aperture photometry (SAP)

<sup>27</sup> <https://mast.stsci.edu>

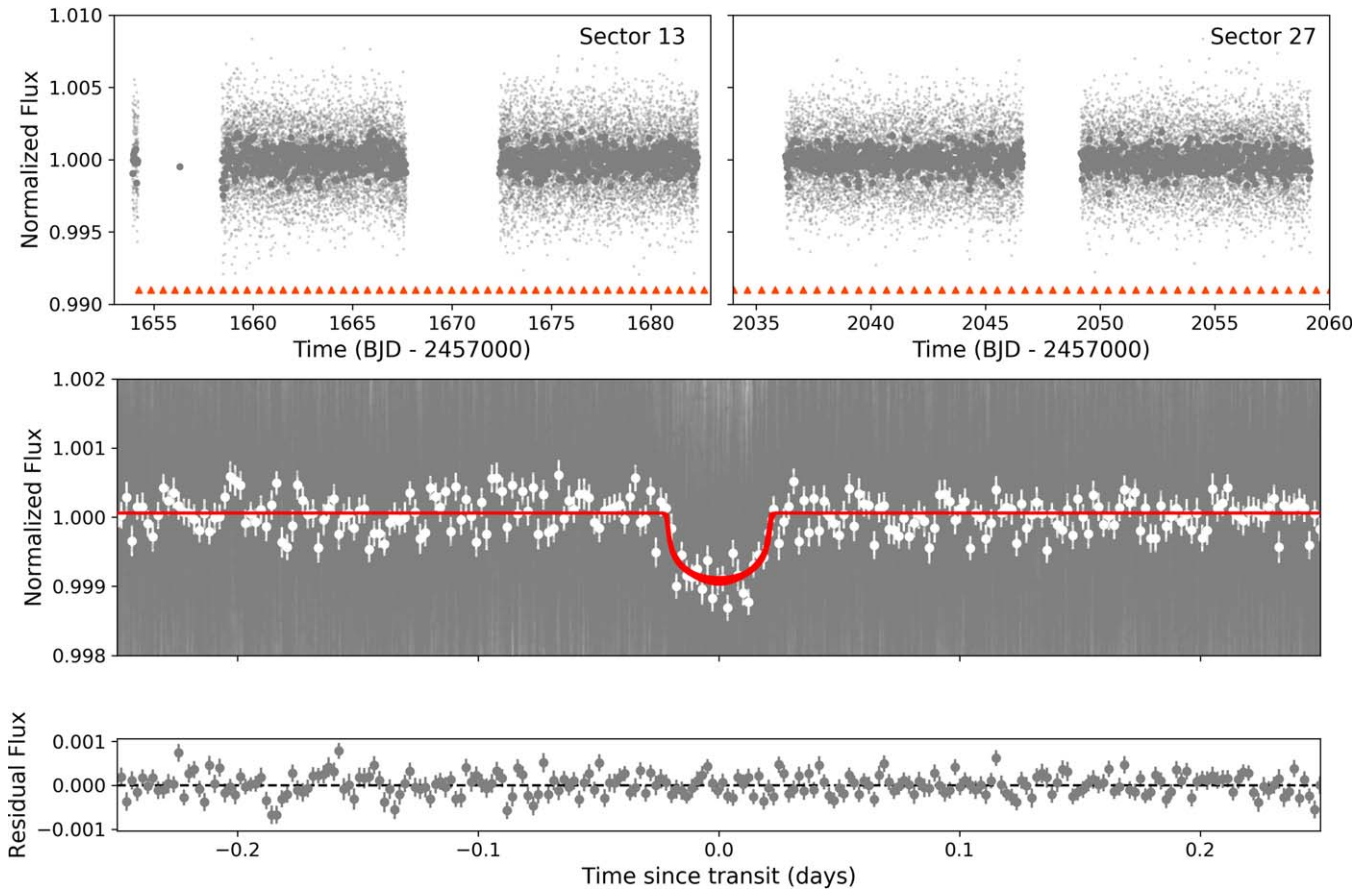


**Figure 4.** TESS light curves of TOI-1075. Top: detrended, normalized, and flattened PDCSAP flux measurements for Sector 13 (left) and Sector 27 (right). Lighter gray points are the TESS 2 minute cadence flux measurements; darker points are the same data binned into 30 minute intervals. The transits of TOI-1075 b are marked by orange triangles. Middle: phase-folded light curve on the planet’s orbital period (0.605 day), along with the best-fit transit model (red). Gray points are 2 minute cadence measurements; white points are the same data binned into 5 minute intervals. Bottom: residuals after the data have been subtracted from the best-fit model.

flux measurements (Twicken et al. 2010; Morris et al. 2017) and presearch data conditioned simple aperture photometry (PDCSAP) flux measurements (Smith et al. 2012; Stumpe et al. 2012, 2014). The instrumental variations present in the SAP flux are removed in the PDCSAP flux data.

We further detrended the TESS PDCSAP data by median normalizing, flattening, fitting a low-order spline, and removing  $3\sigma$  outliers from each sector’s flux measurements separately before stitching the light curves together. The detrended TESS PDCSAP data for Sector 13 and Sector 27, as well as the phase-folded light curve, are shown in Figure 4.

### 3.1.1. TESS Transit Detection

The SPOC Transiting Planet Search (TPS; Jenkins 2002; Jenkins et al. 2010) pipeline searches for threshold crossing events (TCEs) in the PDCSAP light curve, applying an adaptive noise-compensating matched filter to account for stellar variability and residual observation noise. The TCEs with a period of 0.605 day were detected independently in the SPOC transit search of the Sector 13 light<sup>28</sup> Sector 27 light curve, and multisector light curves from Sectors 13 and 27.

In order to rule out false positives that can mimic the planetary transit signal, we evaluated the star’s data validation reports

(DVRs; Twicken et al. 2018; Li et al. 2019), which are generated from the SPOC 2 minute cadence data. The multisector DVR shows no evidence of secondary eclipses, odd/even transit depth inconsistencies, or correlations between the depth of the transit and the size of the aperture used to extract the light curve, which would indicate that the transit signal originated from a nearby eclipsing binary. Additionally, the location of the transit source as shown in the DVR is consistent with the position of the target star; the difference image centroiding test located the source of the transits due to TOI-1075 b to within  $1''.64 \pm 4''.69$  of TOI-1075, which complements the speckle imaging observations. Upon passing these vetting checks, the transit signal was assigned the identifier TOI-1075.01 and announced by the TESS TOI team (Guerrero et al. 2021).

### 3.2. Ground-based Time-series Photometry

After it was alerted as a TOI, we acquired ground-based time-series follow-up photometry of TOI-1075 during future times of transit predicted by the TESS data. We used the TESS Transit Finder, which is a customized version of the Tapir software package (Jensen 2013), to schedule our transit observations.

#### 3.2.1. LCOGT 1 m Observations

We observed five full transits of TOI-1075 in the Pan-STARRS  $z$ -short band from the Las Cumbres Observatory Global Telescope (LCOGT; Brown et al. 2013) 1.0 m network

<sup>28</sup> The gap at the beginning of the TESS Sector 13 data in Figure 4 is a result of cadences being excluded from TPS due to the effects of rapidly changing scattered light and glints from the Earth and Moon.

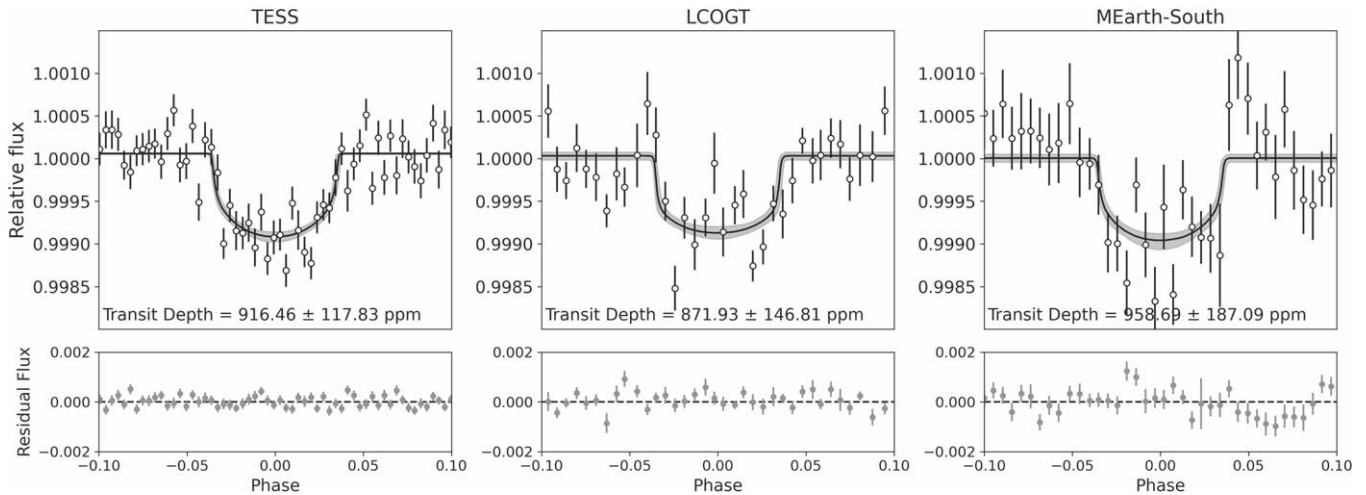


**Figure 5.** Results of the *juliet* joint fit to the TESS photometry and ground-based LCOGT and MEarth-South photometry. Top: transit observations of the respective instruments phase-folded to the period of TOI-1075 b. The black curve is the best-fit *juliet* transit model, and the 68% confidence interval is represented by the gray shaded region. The binned data points with error bars are shown for clarity (white circles). The TESS data are binned in 2 minute intervals, and the LCOGT and MEarth-South data are binned in 5 minute intervals. Bottom: residuals after the data have been subtracted from the best-fit model.

on UTC 2019 August 25, 2019 August 26, 2019 September 23, 2019 September 24, and 2019 September 26 (Figure 5). The first, third, and fifth observations were conducted from the South African Astronomical Observatory node and the second and fourth observations from the Siding Spring Observatory node. The 1 m telescopes are equipped with  $4096 \times 4096$  SINISTRO cameras having an image scale of  $0''.389 \text{ pixel}^{-1}$ , resulting in a  $26' \times 26'$  field of view. The images were calibrated by the standard LCOGT BANZAI pipeline (McCully et al. 2018). Photometric data were extracted using *Astro-ImageJ* (Collins et al. 2017) and circular photometric apertures with radii in the range  $6''.2\text{--}7''.8$ . The target star apertures exclude flux from all known nearby Gaia DR3 and TESS Input Catalog stars. We detect the event on target in all five data sets, which are included in the joint model of the system in this work.

### 3.2.2. MEarth-South 0.4 m Observations

We observed two full transits of TOI-1075 b using the MEarth-South telescope array (Nutzman & Charbonneau 2008; Irwin et al. 2015) at the Cerro Tololo Inter-American Observatory, Chile, on UT 2019 September 22 and 2019 September 28 (Figure 5). Observations were gathered for approximately 5.5 hr centered on the predicted time of mid-transit. The data were reduced using the standard MEarth processing pipeline (e.g., Berta et al. 2012) with a photometric extraction aperture of  $r = 14$  pixels ( $11''.8$ ). Twelve light curves were observed across six telescopes and collected with an RG715 filter. All of the light curves contain meridian flips prior to the predicted time of ingress. These were accounted for in the analysis of the light curves by allowing for separate magnitude zero-points for each combination of telescope and side of the meridian to remove any residual flat-fielding error. Some residuals in the out-of-transit baseline, likely due to color-dependent atmospheric extinction, were found, so the final model also included a linear decorrelation against airmass.

### 3.2.3. Previous Validation of TOI-1075 b

Additionally, planet candidate TOI-1075.01 was statistically validated as a planet using TESS and ground-based photometry

in Gialalone et al. (2022). TOI-1075.01 was vetted with DAVE (Kostov et al. 2019), which uses centroid offset analyses to identify evidence of false positives due to contamination from nearby stars, and TRICERATOPS (Gialalone & Dressing 2020; Gialalone et al. 2021), which calculates the Bayesian probability that the candidate is an astrophysical false positive. TOI-1075.01 showed no strong indicators of being a false positive in the aforementioned analysis and was then validated as TOI-1075 b (Gialalone et al. 2022).

### 3.3. Time-series RVs

We collected 18 precision RV epochs of TOI-1075 using the PFS (Crane et al. 2006, 2008, 2010) on the 6.5 m Magellan II (Clay) telescope at Las Campanas Observatory in Chile. The PFS is a slit-fed spectrograph that is wavelength-calibrated using an iodine cell and covers the wavelength range 391–734 nm, though only the 500–620 nm range is used when measuring RV shifts. All PFS spectra are reduced and RVs extracted using a custom IDL pipeline based on Butler et al. (1996) that regularly delivers sub- $1 \text{ m s}^{-1}$  precision. Each of the 18 PFS TOI-1075 iodine observations consist of  $3 \times 20$  minute exposures and were mostly obtained on a night-by-night basis between UT 2021 May 22 and UT 2021 November 15, although in some cases, two observations were taken on the same night but separated in time by at least 1–2 hr. A 2 hr iodine-free template observation was obtained on UT 2021 May 29. All observations were taken with the default  $0''.3$  slit but in  $3 \times 3$  binning mode, resulting in a resolving power of  $R \sim 110,000$ . The resulting unbinned (20 minutes integration time) RVs have typical precisions of  $2.5\text{--}3.0 \text{ m s}^{-1}$  and are listed in full in Table 2.

A generalized Lomb–Scargle (GLS) periodogram of the PFS RV data shows a significant peak at 0.605 day (Figure 6), which matches the orbital period of the planet candidate determined from the TESS data. An additional significant peak at  $\sim 15$  days likely corresponds to a stellar activity signal. The stellar activity signal is well separated from the planet period, and there are no stellar periodicity signals more dominant than the planet signal or any significant stellar signals that appear around the planet period. Additionally, we modeled the suggested stellar activity signal using a Gaussian process

**Table 2**  
PFS RV Data of TOI-1075

Date (BJD <sub>TDB</sub> )	RV (m s <sup>-1</sup> )	$\sigma_{RV}$ (m s <sup>-1</sup> )
2,459,356.868	-12.48	2.90
2,459,356.884	-5.77	3.04
2,459,356.897	-14.11	2.65
2,459,357.856	-25.83	3.00
2,459,357.870	-8.09	2.52
2,459,357.885	-18.11	3.38
2,459,358.848	-30.56	2.40
2,459,358.862	-26.80	2.18
2,459,358.876	-27.47	2.30
2,459,452.564	-11.29	2.34
2,459,452.578	-11.31	2.49
2,459,452.593	-6.06	2.57
2,459,452.665	-12.61	2.69
2,459,452.679	-5.05	2.56
2,459,452.693	-6.42	3.01
2,459,470.617	10.02	3.18
2,459,470.631	-6.18	3.05
2,459,470.645	1.55	3.65
2,459,471.561	10.02	2.61
2,459,471.576	14.14	2.58
2,459,471.590	13.93	2.55
2,459,471.659	15.38	2.71
2,459,471.673	13.14	2.52
2,459,471.687	6.22	2.58
2,459,473.537	11.41	2.48
2,459,473.550	17.32	2.52
2,459,473.565	20.98	3.25
2,459,473.647	6.82	3.02
2,459,473.661	10.98	3.19
2,459,473.675	14.55	3.39
2,459,474.554	-3.83	2.69
2,459,474.568	4.77	2.62
2,459,474.583	-2.40	3.05
2,459,474.616	6.56	3.00
2,459,474.630	2.55	3.02
2,459,475.526	-5.85	3.07
2,459,475.540	-3.90	2.47
2,459,475.554	-6.89	2.60
2,459,501.537	7.60	2.90
2,459,501.551	-2.56	2.80
2,459,501.565	4.48	2.86
2,459,504.528	0.00	2.47
2,459,504.542	-9.94	2.75
2,459,504.556	-12.43	2.91
2,459,505.549	11.69	4.34
2,459,505.563	7.41	3.99
2,459,505.578	4.74	3.25
2,459,506.518	-19.93	2.41
2,459,506.532	-1.76	2.45
2,459,506.546	-14.89	2.33
2,459,531.523	7.30	2.49
2,459,531.537	10.63	2.55
2,459,533.536	7.42	2.67
2,459,533.546	11.35	4.27

(GP) and find no evidence to incorporate it into our final model (see Section 4.2.1). Therefore, incorporating GPs for non-white-noise models or adding another term to our RV model fit was deemed unnecessary.

#### 4. System Parameters from juliet

To obtain the precise parameters of the TOI-1075 system, we performed a joint analysis of the TESS, LCOGT, and MEarth-

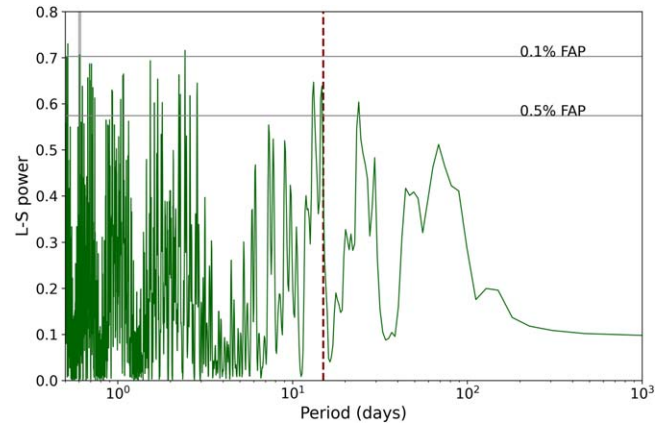


**Figure 6.** The GLS periodogram of the RV measurements from PFS. There is a clear peak at the period of TOI-1075 b (gray bar). We identify a stellar activity signal at  $\sim 15$  days (red dashed line) that is well separated from TOI-1075 b’s orbital period.

South photometry and the PFS RV data using `juliet` (Espinoza et al. 2019). The fitting tool `juliet` uses nested sampling algorithms to efficiently sample a given parameter space and allows for model comparison based on Bayesian evidence. The `juliet` tool combines the publicly available packages for transits and RV modeling, `batman` (Kreidberg 2015) and `radvel` (Fulton et al. 2018), respectively. We opted to implement `dynesty` (Speagle 2020) as the nested sampling algorithm for our joint fitting, though a range of nested sampling algorithms are available to choose from.

#### 4.1. Transit Modeling

For the transit modeling, `juliet` employs the `batman` package. We adopt a quadratic model to describe the limb-darkening effect in the TESS, LCOGT, and MEarth-South photometry and parameterize it by employing the efficient, uninformative sampling scheme of Kipping (2013) and a quadratic law. We used a fixed dilution factor of 1 for all instruments but considered free individual instrumental offsets. Instrumental jitter terms were taken into account and added in quadrature to the nominal instrumental error bars. We used uniform priors per the Espinoza (2018) parameterization to explore the full physically plausible parameter space for the planet-to-star radius ratio,  $p = R_p/R_*$ , and impact parameter,  $b$ . Additionally, we defined a log-uniform prior on the stellar density and then recovered the scaled semimajor axis ( $a/R_*$ ) using Kepler’s third law.

#### 4.2. RV Modeling

The model that we selected for our RV joint fit analysis was composed of a circular Keplerian orbit for the transiting planet (USP planets are expected to be tidally circularized) and an additional linear long-term trend to constrain the non-Keplerian long-period signal present in the PFS RV data, whose period is longer than the current observation baseline. We assumed uniform wide priors for the systemic velocity, jitter term, and RV semiamplitude of the PFS RVs, as well as the linear long-term trend parameterized by an intercept  $B$  and a slope  $A$ . We measured an RV semiamplitude of  $K = 10.95^{+1.50}_{-1.43}$  m s<sup>-1</sup> for TOI-1075 b.

#### 4.2.1. RV Model Comparison

`juliet` searches for the global posterior maximum based on the evaluation of the Bayesian log-evidence ( $\ln \mathcal{Z}$ ), allowing us to perform model comparisons given the differences in  $\Delta \ln \mathcal{Z}$ . We modeled the PFS RV data with and without fitting a linear long-term trend to the data. The model with the linear long-term trend had a log-evidence of  $\ln \mathcal{Z} = -204.01 \pm 0.38$ , and the model without the linear long-term trend (a circular Keplerian model only) had a log-evidence of  $\ln \mathcal{Z} = -212.95 \pm 0.28$ , resulting in  $\Delta \ln \mathcal{Z} = 8.94$ . We selected the model with the linear long-term trend component following criteria described in Trotta (2008), which consider  $\Delta \ln \mathcal{Z} > 2$  as weak evidence that one model is preferred over the other and  $\Delta \ln \mathcal{Z} > 5$  as strong evidence that one model is significantly preferred over the other; hence, the additional model parameters are necessary to account for the long-period signal in the PFS RV data. We also considered a model composed of a circular Keplerian orbit and a long-term trend parameterized by an intercept  $B$ , a slope  $A$ , and a quadratic/curvature coefficient  $Q$ . The change in log-evidence was  $\Delta \ln \mathcal{Z} < 2$  between the long-term trend parameterization with and without the additional parameter,  $Q$ , confirming that the RV data are legitimately fitted by a circular Keplerian model and a linear long-term trend. As an additional test, we added a stellar signal to the RV model using a GP to determine the effect of the 15 day period signal identified in the PFS GLS periodogram (Figure 6). We compared the models with and without the additional stellar signal and found no evidence ( $\Delta \ln \mathcal{Z} < 2$ ) that the final model required the addition of a stellar signal.

We show the final transit and RV models of the joint fit based on the posterior sampling in Figures 5 and 7, respectively; the posterior parameters of our joint fit in Table 3; the selected priors for our joint fit in Table A1; the obtained posterior probabilities in Figure A1; and the derived planetary parameters of TOI-1075 b based on the posteriors of the joint fit in Table 4.

To summarize, the TOI-1075 system consists of a late-K/early-M-dwarf host star with at least one hot super-Earth planet, TOI-1075 b (see Table 4), which has a mass of  $M_p = 9.95^{+1.36}_{-1.30} M_{\oplus}$  and radius of  $R_p = 1.791^{+0.116}_{-0.081} R_{\oplus}$  on a circular orbit with a period of 0.605 day. We derived a bulk density of  $\rho = 9.32^{+2.05}_{-1.85} \text{ g cm}^{-3}$  and an equilibrium temperature, assuming a zero albedo, of  $T_{\text{eq}} = 1323 \pm 44 \text{ K}$ .

## 5. Discussion

Our RV measurements of TOI-1075 b constrain the planetary mass with an uncertainty of  $\sim 14\%$ , and the TESS, LCOGT, and MEarth-South light curves constrain the planetary radius with an uncertainty of  $\sim 7\%$ . Thus, TOI-1075 b belongs to the small group of super-Earths with precisely measured masses<sup>29</sup> and radii, or those planets with measurement precision better than 30% (see Figure 8). With precise mass and radius measurements in hand for TOI-1075 b, we discuss implications for radius valley studies, the potential for planetary atmospheric characterization, potential planetary compositions, planetary bulk density, and possible planet formation mechanisms. We also discuss constraints on a potential second planet in the TOI-1075 system.

### 5.1. Implications for the Radius Valley around M Dwarfs

Several physical mechanisms/theoretical models have been proposed to explain the existence of the radius gap. These mechanisms include thermally driven atmospheric mass loss, e.g., photoevaporation (Lopez et al. 2012; Chen & Rogers 2016; Owen & Wu 2017) and core-powered mass loss (Ginzburg et al. 2018; Gupta & Schlichting 2019, 2020), and gas-poor formation, a natural outcome of planet formation, where rocky super-Earths are a result of formation in gas-poor environments without requiring any atmospheric escape (Lee et al. 2014; Lee & Chiang 2016; Lopez & Rice 2018; Lee & Connors 2021). The slope of the radius valley (in period–radius space) can be used to discern between a thermally driven mass-loss model or a gas-poor formation model (Lopez & Rice 2018; Gupta & Schlichting 2020; Lee & Connors 2021).

The slope of the radius valley around Sun-like stars has been characterized using data from the Kepler and K2 missions, and both thermally driven mass-loss and gas-poor formation models are favored in this stellar-mass regime (Van Eylen et al. 2018; Martinez et al. 2019). However, around low-mass mid-K to mid-M dwarfs, Cloutier & Menou (2020) found tentative evidence that the slope of the radius valley is consistent with predictions from gas-poor formation. Additionally, the radius gap decreases as stellar radius decreases, and the radius gap is centered at  $1.54 \pm 0.16 R_{\oplus}$  for low-mass K and M-dwarf stars (versus  $1.75 R_{\oplus}$  for Sun-like stars in Fulton et al. 2017).

TOI-1075 b lies between the predicted slopes of the thermally driven mass-loss model and gas-poor formation model and hence within the M-dwarf radius valley created by these mechanisms (the M-dwarf radius valley ranges from 1.5 to  $2.5 R_{\oplus}$  between the predicted slopes; see Figure 9 in Cloutier et al. 2021). TOI-1075 b’s orbital period (0.605 day) and size ( $1.791^{+0.116}_{-0.081} R_{\oplus}$ ) make it a “keystone planet,” a valuable target to conduct tests of competing radius valley models across a range of stellar masses using precise planetary mass and radius measurements (Cloutier & Menou 2020). TOI-1075 b joins TOI-1235 b (Bluhm et al. 2020; Cloutier et al. 2020), TOI-776 b (Luque et al. 2021), TOI-1685 b (Bluhm et al. 2021), and TOI-1634 b (Cloutier et al. 2021) as keystone planets that will help elucidate the physical mechanism that formed the radius valley around early-M dwarfs. Distinguishing between the two atmospheric loss mechanisms will require the discovery of additional keystone planets for statistical studies and population analysis, as well as atmospheric studies of TOI-1075 b and other keystone planets to provide observational evidence to validate model predictions.

### 5.2. Atmospheric Characterization Prospects

Super-Earths with  $R_p > 1.6 R_{\oplus}$  are expected to have a substantial H/He atmosphere (Rogers 2015), and though TOI-1075 b’s radius ( $1.791^{+0.116}_{-0.081} R_{\oplus}$ ) places it just above the radius gap, its bulk density is inconsistent with the presence of a low mean molecular weight envelope. Based on TOI-1075 b’s predicted composition (see Section 5.3) and USP, we do not expect the planet to have retained a H/He envelope. But TOI-1075 b could have no atmosphere (bare rock); a metal/silicate vapor atmosphere with a composition set by the vaporizing magma ocean on the surface (Schaefer & Fegley 2009; Ito et al. 2015), since TOI-1075 b’s equilibrium temperature is hot enough to melt a rocky surface

<sup>29</sup> Only planet masses measured by the RV method are considered in order to avoid differences in the planet mass distribution with other methods.

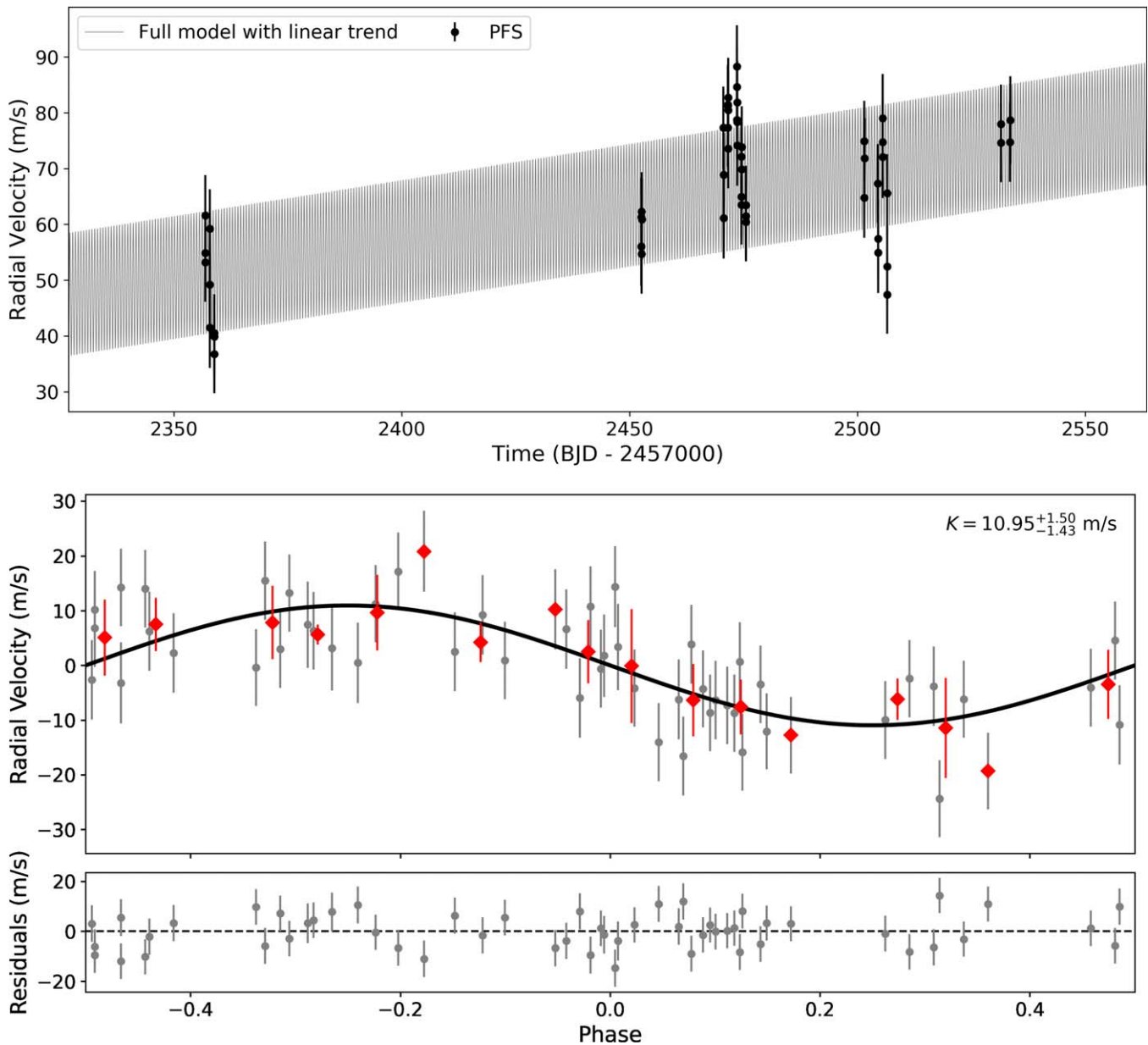


**Figure 7.** Results of the *juliet* joint fit to the PFS RVs. Top: PFS RVs over time (black points) and full best-fit *juliet* model (gray curve). Middle: phase-folded RV measurements from PFS. The black curve is the best-fit *juliet* RV model, the gray points are the unbinned RVs, and the red diamonds are the RV measurements binned in 0.05 units of orbital phase. Error bars are the quadrature sum of the PFS internal uncertainties and the RV jitter estimate from the *juliet* fit. The best-fit RV semi-amplitude is  $K = 10.95^{+1.50}_{-1.43} \text{ m s}^{-1}$ . Bottom: RV residuals after the data have been subtracted from the best-fit model.

(Mansfield et al. 2019); or, especially at the low end of its allowed mean density range, possibly a thin H/He, CO<sub>2</sub>, or other atmosphere. A detailed atmospheric model is needed to determine possible atmospheric compositions for TOI-1075 b, which is beyond the scope of this work.

We calculated the emission spectroscopy metric (ESM) and transmission spectroscopy metric (TSM), as defined by Kempton et al. (2018), to determine TOI-1075 b’s potential for atmospheric characterization. Using the stellar parameters reported in Section 2.2 and the planetary parameters in Table 4, we obtain  $\text{ESM} = 10.1 \pm 1.6$  and  $\text{TSM} = 29 \pm 8$ .

TOI-1075 b is a good candidate for emission spectroscopy with the JWST. The planet may have a mineral-rich atmosphere consisting of metal and silicate vapors, since its equilibrium temperature is high enough to melt silicate rock (Schaefer & Fegley 2009; Léger et al. 2011; Ito et al. 2015;

Ito & Ikoma 2021). If TOI-1075 b has no atmosphere, its surface may be characterized via secondary eclipse observations. With an ESM value of  $10.1 \pm 1.6$ , TOI-1075 b is well above the threshold ESM of 7.5 suggested by Kempton et al. (2018) for a high-quality atmospheric characterization target. It is one of only eight super-Earths, including 55 Cancri e (Bourrier et al. 2018), HD 213885 b (Espinoza et al. 2020), HD 3167 b (Christiansen et al. 2017), TOI-431 b (Osborn et al. 2021), TOI-500 b (Serrano et al. 2022), TOI-1807 b (Nardiello et al. 2022), and K2-141 b (Malavolta et al. 2018), with mass measurement precision  $>5\sigma$  and  $V/J/H/K < 13$  mag, that has an  $\text{ESM} > 7.5$ . It is also the only super-Earth above the radius gap in the temperature range 1250–1750 K,<sup>30</sup> which will allow us to probe an intermediate temperature range of hot super-

<sup>30</sup> <https://tess.mit.edu/science/tess-acwg/> (as of 2022 October 5).

**Table 3**  
Median Values and 68% Confidence Interval for Posterior Parameters from Joint Photometric and RV *juliet* Analysis for the TOI-1075 System

Parameter	Units	Values		
Stellar Parameters				
$\rho_*$	Density ( $\text{g cm}^{-3}$ )	$3.73^{+0.99}_{-1.67}$		
Planet Parameters				
TOI-1075 b				
$P$	Period (days)	$0.6047328 \pm 0.0000032$		
$T_0$	Time of transit center ( $\text{BJD}_{\text{TDB}}$ )	$2,458,654.2510^{+0.00040}_{-0.00050}$		
$r_1$	Parameterization of Espinoza (2018) for $b$	$0.60^{+0.20}_{-0.17}$		
$r_2$	Parameterization of Espinoza (2018) for $R_p/R_*$	$0.0282^{+0.0019}_{-0.0013}$		
$K$	RV semiamplitude ( $\text{m s}^{-1}$ )	$10.95^{+1.50}_{-1.43}$		
$e$	Eccentricity (fixed)	0.00		
Photometry Parameters				
		MEarth-South	LCOGT	TESS
$M$	Relative flux offset	0.0000	0.0000	-0.0001
$\sigma$	Jitter term for light curve (ppm)	$901.29^{+86.80}_{-91.69}$	$471.24^{+58.31}_{-62.17}$	$3.21^{+25.84}_{-2.86}$
$q_1$	Quadratic limb-darkening parameterization (Kipping 2013)	$0.54^{+0.28}_{-0.31}$	$0.34^{+0.33}_{-0.23}$	$0.59^{+0.24}_{-0.25}$
$q_2$	Quadratic limb-darkening parameterization (Kipping 2013)	$0.47^{+0.33}_{-0.30}$	$0.39^{+0.35}_{-0.27}$	$0.47^{+0.29}_{-0.28}$
RV Parameters				
$\mu_{\text{PFS}}$	Systemic velocity for PFS ( $\text{m s}^{-1}$ )	$-67.3^{+24.7}_{-20.1}$		
$\sigma_{\text{PFS}}$	Jitter term for PFS ( $\text{m s}^{-1}$ )	$6.60^{+0.81}_{-0.69}$		
$A$	Slope of linear long-term RV trend ( $\text{m s}^{-1} \text{day}^{-1}$ )	$0.130^{+0.017}_{-0.018}$		
$B$	Intercept of linear long-term RV trend ( $\text{m s}^{-1}$ )	$-67.3^{+23.1}_{-20.6}$		

**Table 4**  
Median Values and 68% Confidence Interval for Derived Parameters from Joint Photometric and RV *juliet* Analysis for TOI-1075 b

Parameter	Units	Values		
Derived Transit Parameters				
$p = R_p/R_*$	Radius of planet in stellar radii	$0.0282^{+0.0019}_{-0.0013}$		
$a/R_*$	Semimajor axis in stellar radii	$4.40^{+0.89}_{-0.91}$		
$b = (a/R_*)\cos(i_p)$	Transit impact parameter	$0.40^{+0.29}_{-0.25}$		
$i_p$	Inclination (deg)	$84.67^{+3.34}_{-3.93}$		
		MEarth-South	LCOGT	TESS
$u_1$	Linear limb-darkening coefficient	$0.61^{+0.52}_{-0.40}$	$0.39^{+0.46}_{-0.27}$	$0.68 \pm 0.39$
$u_2$	Quadratic limb-darkening coefficient	$0.035^{+0.043}_{-0.041}$	$0.10^{+0.32}_{-0.37}$	$0.042^{+0.044}_{-0.039}$
Derived Physical Parameters				
TOI-1075 b				
$R_p$	Radius ( $R_\oplus$ )	$1.791^{+0.116}_{-0.081}$		
$M_p$	Mass ( $M_\oplus$ )	$9.95^{+1.36}_{-1.30}$		
$\rho_p$	Density ( $\text{g cm}^{-3}$ )	$9.32^{+2.05}_{-1.85}$		
$a$	Semimajor axis (au)	$0.01159^{+0.00023}_{-0.00020}$		
$T_{\text{eq}}$	Equilibrium temperature (K)	$1323 \pm 44$		
$g_p$	Surface gravity ( $\text{m s}^{-2}$ )	$30.0^{+5.4}_{-4.8}$		
$S_p$	Insolation ( $S_\oplus$ )	$509.2^{+18.7}_{-20.4}$		

Earths and explore the atmospheric species that have volatilized in this regime.

In addition to having an ESM value above the suggested threshold, TOI-1075 b can also be observed by JWST for  $\sim 200$  days per year. Thus, TOI-1075 b is accessible to JWST for a significant portion of the year, which allows for more flexibility when planning observations.

Kempton et al. (2018) suggested that  $\text{TSM} > 90$  be used as the threshold for planets with  $1.5 R_\oplus < R_p < 10 R_\oplus$ . TOI-1075 b does not meet this criterion because, due to its high mass and hence high surface gravity, it is unlikely to have an extended atmosphere that can be probed in transmission.

### 5.3. Planetary Composition and Density

The measured mass and radius of TOI-1075 b result in a planetary bulk density of  $9.32^{+2.05}_{-1.85} \text{ g cm}^{-3}$ , which is almost twice as dense as the Earth ( $\rho_\oplus = 5.51 \text{ g cm}^{-3}$ ). Comparing TOI-1075 b with the theoretical composition models of Zeng et al. (2021) and Z. Lin et al. (2022, in preparation), the planet's bulk density is consistent with a 35% Fe + 65% silicates by mass composition (see Figure 8).

To simulate TOI-1075 b's interior, we numerically integrate three equations—the mass of a spherical shell, hydrostatic equilibrium, and the equation of state (EOS)—from the planet's center to the surface with a step size of 100 m using a planetary

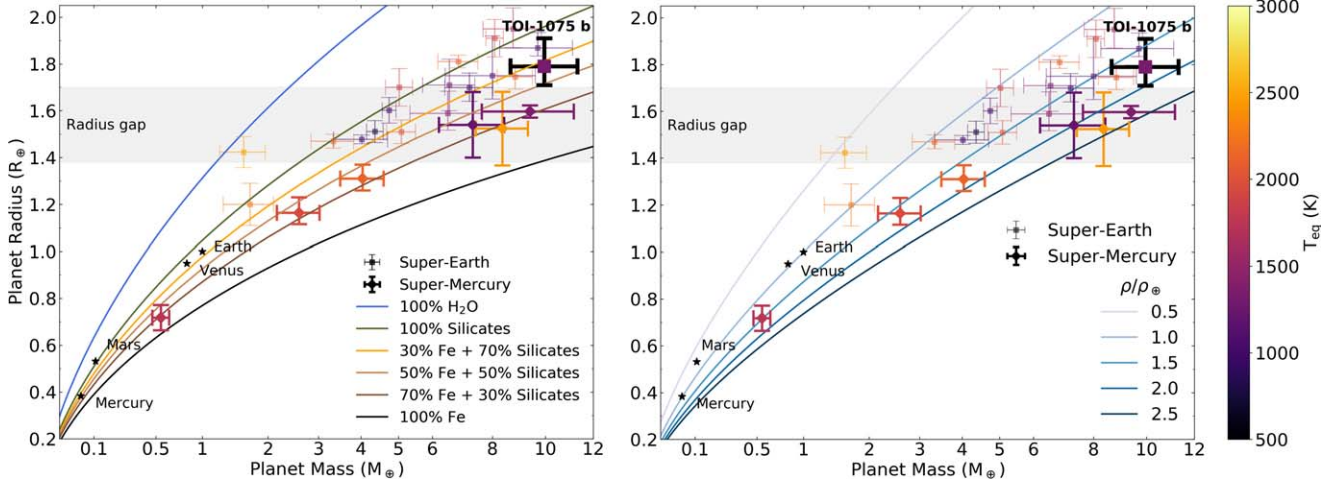


**Figure 8.** Mass–radius diagram for small planets ( $R_p < 2 R_\oplus$  and  $M_p < 10 M_\oplus$ ) with measured mass and radius uncertainties below 30%, as listed in the NASA Exoplanet Archive (only planet masses measured by the RV method are considered). Planets are colored according to their calculated equilibrium temperature (assuming zero albedo and efficient heat redistribution). Super-Earth planets are shown with squares, and super-Mercury planets are shown with diamonds. The gray shaded region denotes the radius gap for low-mass stars centered at  $1.54 \pm 0.16 R_\oplus$  (Cloutier & Menou 2020). The terrestrial solar system planets are plotted for reference. Left: mass–radius diagram with curves of constant composition. The solid lines are theoretical internal composition curves (Zeng et al. 2021; Lin et al. 2022, in preparation). From top to bottom: 100% H<sub>2</sub>O (blue), 100% silicates (green), a mixture of 30% Fe and 70% silicates by mass (orange), a mixture of 50% Fe and 50% silicates by mass (light brown), a mixture of 70% Fe and 30% silicates by mass (dark brown), and 100% Fe (black). The bulk density of TOI-1075 b is consistent with a 35% Fe + 65% silicates by mass composition. Right: mass–radius diagram with curves of constant density relative to Earth. The density of TOI-1075 b is  $\sim 1.75$  times greater than the Earth.

interior simulation code (Lin et al. 2022, in preparation). The code is validated against recent mass–radius curves calculated by Zeng et al. (2021). We assume a completely differentiated planet with an iron core and a mantle consisting of silicates. For iron and silicates, we adopt a second-order adapted polynomial EOS developed by Holzappel (2018) using EOS coefficients listed in Zeng et al. (2021). The inner boundary conditions of the simulated planets are assumed to be  $M(0) = 0$  and  $P(0) = P_c$ , where  $P_c$  is the central pressure. We switch from the iron core to the silicate mantle when the desired core mass has been reached. The iteration terminates when the outer boundary condition  $P(R) \leq 1$  bar is satisfied. We use a bisection method to search for the  $P_c$  that produces  $M(R) = M_p$  for a given core-mass fraction (CMF). Using the mean measured mass and radius of TOI-1075 b, we compute a mean CMF of 0.35. We then calculate a core-radius fraction (CRF) by dividing the radius of the iron layer by the total radius of the planet, resulting in a mean CRF of 0.52, or  $0.93 R_\oplus$ .

We further consider the most and least dense scenarios permissible by the mass and radius error bars. In the most dense scenario ( $M_p = 11.31 M_\oplus$ ,  $R_p = 1.709 R_\oplus$ ), we compute a CMF of 0.61 and a CRF of 0.67, or  $1.15 R_\oplus$ . In the least dense scenario ( $M_p = 8.65 M_\oplus$ ,  $R_p = 1.91 R_\oplus$ ), even a coreless pure silicates composition (CMF = 0, CRF = 0) cannot explain the low-end density of the planet. Even though such a coreless planet is unphysical from a planet formation perspective, we include this extreme scenario for completeness.

Though we have precisely measured the mass of TOI-1075 b to  $>7\sigma$  ( $9.95^{+1.36}_{-1.30} M_\oplus$ ), the uncertainty on the mass measurement leads to a wide range of possible CMF ( $0.35^{+0.26}_{-0.35}$ ) and CRF ( $0.52^{+0.15}_{-0.52}$ ) values, which can only be resolved with more precise mass and radius measurements not currently available. In the following sections, we discuss possible formation scenarios that could result in the mean density, most dense, and least dense scenarios.

### 5.3.1. TOI-1075 b’s Mean Density and Composition

The mean mass and radius ( $M_p = 9.95 M_\oplus$ ,  $R_p = 1.791 R_\oplus$ ) of TOI-1075 b result in a bulk density of  $9.32 \text{ g cm}^{-3}$ . While TOI-1075 b’s mean bulk density is  $\sim 1.75 \times$  that of Earth, its mean CMF (0.35) and CRF (0.52) are consistent with a predominantly rocky, Earth-like composition and internal structure. Its uncompressed density is  $4.91 \text{ g cm}^{-3}$ , which is similar to the uncompressed density of the Earth ( $4.79 \text{ g cm}^{-3}$ ), further supporting our findings of an Earth-like composition for TOI-1075 b.

TOI-1075 b is the most massive and densest super-Earth with  $1.6 R_\oplus < R_p < 2 R_\oplus$  discovered to date. The similarity in TOI-1075 b’s CMF relative to Earth (CMF<sub>⊕</sub> = 32.5%; Seager et al. 2007) supports our finding that TOI-1075 b likely lacks a massive low mean molecular weight envelope, which, if present, would have corresponded to a larger observed radius for a given mass.

A handful of massive terrestrial planets like TOI-1075 b have been discovered, but these objects are relatively rare. Planets similar in radius and Earth-like composition to TOI-1075 b are listed in Table 5.

### 5.3.2. TOI-1075 b as a Super-Mercury

In the most dense scenario ( $M_p = 11.31 M_\oplus$ ,  $R_p = 1.710 R_\oplus$ ,  $\rho = 11.37 \text{ g cm}^{-3}$ ), we consider the possibility of TOI-1075 b as a super-Mercury. The term “super-Mercury” generally refers to planets that are super-Earth-sized with enhanced uncompressed bulk densities, as compared to Earth-like planets. The high density has been interpreted to be indicative of a high iron-mass fraction, analogous to the solar system planet Mercury (Marcus et al. 2010; Adibekyan et al. 2021), and the formation mechanism for these planets is still unknown. Based on TOI-1075 b’s bulk density ( $9.32^{+2.05}_{-1.85} \text{ g cm}^{-3}$ ), if the planet’s mass is in the high range, with a high CMF in the allowed range (CMF =  $0.35^{+0.26}_{-0.35}$ ), it could be a super-Mercury. The small group of recently identified super-Mercuries includes

**Table 5**  
Massive Terrestrial Planet Parameters

Planet Name	Planet Radius ( $R_{\oplus}$ )	Planet Mass ( $M_{\oplus}$ )	$T_{\text{eq}}$ (K)	References
TOI-1075 b	$1.791^{+0.116}_{-0.081}$	$9.95^{+1.36}_{-1.30}$	$1323 \pm 44$	This work
Kepler-20 b	$1.868^{+0.066}_{-0.034}$	$9.70^{+1.41}_{-1.44}$	$1105 \pm 37$	Buchhave et al. (2016)
LHS 1140 b	$1.727 \pm 0.032$	$6.98 \pm 0.89$	$235 \pm 5$	Ment et al. (2019)
TOI-1235 b	$1.738^{+0.087}_{-0.076}$	$6.91^{+0.75}_{-0.85}$	$754 \pm 18$	Cloutier et al. (2020)
HD 213885 b	$1.74 \pm 0.05$	$8.8 \pm 0.6$	$2128 \pm 14$	Espinoza et al. (2020)
WASP-47 e	$1.808 \pm 0.026$	$6.77 \pm 0.57$	$2514 \pm 70$	Bryant & Bayliss (2022)
K2-216 b	$1.72 \pm 0.06$	$8.18 \pm 1.65$	$1217 \pm 34$	Clark et al. (2022)

K2-38 b, K2-106 b, K2-229 b, Kepler-107 c, and Kepler-406 b (Adibekyan et al. 2021), as well as GJ 367 b (Lam et al. 2021) and HD 137496 b (Silva et al. 2022), which are represented by bold data points in Figure 8.

We investigated possible formation mechanisms that could result in the high density and CMF and CRF ranges observed for TOI-1075 b, including giant impacts (Benz et al. 2008; Marcus et al. 2010; Asphaug & Reufer 2014; Liu et al. 2015; Scora et al. 2020; Cambioni et al. 2021, 2022), in situ formation (Weidenschilling 1978; Kruss & Wurm 2018; Johansen & Dorn 2022), an initially metal-rich protoplanetary disk composition (Veyette et al. 2017; Adibekyan et al. 2021; Schulze et al. 2021; Souto et al. 2022), and the decompressed core of an evaporated gas giant (Hébrard et al. 2003; Mocquet et al. 2014), but we do not have sufficient information to resolve the planet’s formation mechanism.

### 5.3.3. TOI-1075 b as a Low-density Planet

In the least dense scenario ( $M_p = 8.65 M_{\oplus}$ ,  $R_p = 1.907 R_{\oplus}$ ,  $\rho = 7.47 \text{ g cm}^{-3}$ ), our interior model results in a coreless silicate planet and requires an additional water layer to account for the inflated radius. Such a coreless planet is unphysical from a planet formation perspective; a planet with a mass of TOI-1075 b is expected to have fully differentiated, e.g., Rubie et al. (2015) and Cambioni et al. (2021). A water layer would be physically unstable at TOI-1075 b’s equilibrium temperature. Therefore, layers less dense than silicates must be added to the model to fit the minimum mass and maximum radius scenario. Possible candidates for these layers include low-pressure silicate phases or a metal/silicate vapor atmosphere.

### 5.4. A Potential Second Planet in the System

We find a linear long-term trend in the PFS RV data (see Section 4.2) whose period is longer than the baseline of our RV observations. This may indicate the presence of a second planet in the system. We place lower limits on the period, semiamplitude, and mass of a second planet candidate as the source of the long-term trend.

The orbital period of the second planet candidate is at least twice the observing baseline of the PFS RV observations (otherwise we would have seen the RV trend turn over before our observations concluded as the potential planet passed through its quadrature phase). The PFS observations were taken over a period of 176.68 days ( $T_{\text{baseline}}$ ); hence, the orbital period of the planet candidate should be at least 353 days.

Taking the best-fit linear trend results from `juliet`, the RV data are shifted  $0.130^{+0.017}_{-0.018} \text{ m s}^{-1} \text{ day}^{-1}$ . Thus, the RV semiamplitude of the planet candidate must be at least  $(T_{\text{baseline}} \times \text{RV trend})/2 = 11.48 \text{ m s}^{-1}$ .

Combining the minimum orbital period (353 days) and RV semiamplitude ( $11.48 \text{ m s}^{-1}$ ) and assuming a circular Keplerian orbit, the minimum mass of the second planet candidate is  $\sim 87 M_{\oplus}$ , or  $\sim 0.28 M_{\text{Jupiter}}$ .

The presence of a second planet candidate motivates us to collect additional RV data for this system in order to determine the period and measure the mass of the second planet candidate while also improving the uncertainty on the mass measurement of TOI-1075 b. Additionally, there are currently a handful of systems consisting of a USP planet and a close-in companion with periods ranging from a few days to tens of days, e.g., K2-106 (Guenther et al. 2017), K2-141 (Malavolta et al. 2018), K2-229 (Santerne et al. 2018), and TOI-500 (Serrano et al. 2022). These close-in companions could be responsible for migrating the USP planets to their current positions (Pu & Lai 2019; Millholland & Spalding 2020; Serrano et al. 2022). The possible existence of such a close-in companion in the TOI-1075 system serves as additional motivation for further RV follow-up of the system.

Determining the source (possibly a second planet) of the long-term radial-velocity trend, and more accurately measuring TOI-1075 b’s planet mass and parameters will further detailed planet formation, planet migration and atmospheric characterization efforts, since a planet’s gravity plays an important role in its collisional history and interpreting atmospheric spectra (Batalha et al. 2019).

## 6. Conclusions

We report the discovery and confirmation of TOI-1075 b, a transiting, ultra-short-period hot super-Earth orbiting a nearby ( $d = 61.4 \text{ pc}$ ) late-K/early-M-dwarf star. Using photometric observations from TESS, LCOGT, and MEarth-South and RV observations from PFS, we precisely measure the radius and mass of TOI-1075 b to be  $1.791^{+0.116}_{-0.081} R_{\oplus}$  and  $9.95^{+1.36}_{-1.30} M_{\oplus}$ , respectively. Our PFS RV data also suggest the presence of a second planet candidate in the system, with a minimum mass of  $\sim 87 M_{\oplus}$  and a minimum orbital period of  $\sim 353$  days. TOI-1075 b has a bulk density of  $9.32^{+2.05}_{-1.85} \text{ g cm}^{-3}$ , consistent with a composition of 35% iron by mass, and a CRF of 52%. It is a good candidate for emission spectroscopy with JWST, which we can use to characterize a potentially mineral-rich atmosphere. TESS is scheduled to observe TOI-1075 again in Year 5, Sector 67 (July 2023), which will provide a more precise planet radius and the ability to search for variations in the planet period on a 4 yr timescale. TOI-1075 b is a massive, dense, high-temperature, ultra-short-period super-Earth inside the M-dwarf radius valley, making the system ideal for testing planet formation and evolution theories, density-enhancing mechanisms, and theoretical models related to atmospheric loss.

This paper includes data collected by the TESS mission. Funding for the TESS mission is provided by NASA’s Science Mission directorate. This paper includes data gathered with the 6.5 m Magellan Telescopes located at Las Campanas Observatory, Chile. This work makes use of observations from the LCOGT network. Part of the LCOGT telescope time was granted by NOIRLab through the Mid-Scale Innovations Program (MSIP). The MSIP is funded by NSF. This work has made use of data from the European Space Agency (ESA) mission Gaia (<https://www.cosmos.esa.int/gaia>), processed by the Gaia Data Processing and Analysis Consortium (DPAC; <https://www.cosmos.esa.int/web/gaia/dpac/consortium>). Funding for the DPAC has been provided by national institutions, in particular the institutions participating in the Gaia Multilateral Agreement. Some of the observations in the paper made use of the High-Resolution Imaging instrument Zorro obtained under Gemini LLP proposal No. GN/S-2021A-LP-105. Zorro was funded by the NASA Exoplanet Exploration Program and built at the NASA Ames Research Center by Steve B. Howell, Nic Scott, Elliott P. Horch, and Emmett Quigley. Zorro was mounted on the Gemini North (and/or South) telescope of the international Gemini Observatory, a program of NSF’s OIR Lab, which is managed by the Association of Universities for Research in Astronomy (AURA) under a cooperative agreement with the National Science Foundation on behalf of the Gemini partnership: the National Science Foundation (United States), National Research Council (Canada), Agencia Nacional de Investigación y Desarrollo (Chile), Ministerio de Ciencia, Tecnología e Innovación (Argentina), Ministério da Ciência, Tecnologia, Inovações e Comunicações (Brazil), and Korea Astronomy and Space Science Institute (Republic of Korea). The MEarth Team gratefully acknowledges funding from the David and Lucile Packard Fellowship for Science and Engineering (awarded to D. C.). This material is based upon work supported by the National Science Foundation under grants AST-0807690, AST-1109468, AST-1004488 (Alan T. Waterman Award), and AST-1616624 and the National Aeronautics and Space Administration under grant No. 80NSSC18K0476 issued through the XRP Program. This work is made possible by a grant from the John Templeton Foundation. The opinions expressed in this publication are those of the authors and do not necessarily reflect the views of the John Templeton Foundation. Resources supporting this work were provided by the NASA High-End Computing (HEC) Program

through the NASA Advanced Supercomputing (NAS) Division at Ames Research Center for the production of the SPOC data products. This research was carried out in part at the Jet Propulsion Laboratory, California Institute of Technology, under a contract with the National Aeronautics and Space Administration (80NM0018D0004). Some of the data presented in this paper were obtained from the Mikulski Archive for Space Telescopes (MAST). The specific observations analyzed can be accessed via [10.17909/t9-wpz1-8s54](https://doi.org/10.17909/t9-wpz1-8s54). This research has made use of the NASA Exoplanet Archive (DOI:[10.26133/NEA12](https://doi.org/10.26133/NEA12)), made available by the NASA Exoplanet Science Institute at IPAC, which is operated by the California Institute of Technology under contract with the National Aeronautics and Space Administration. This research has made use of NASA’s Astrophysics Data System. This research has made use of the Exoplanet Follow-up Observation Program (DOI:[10.26134/ExoFOP5](https://doi.org/10.26134/ExoFOP5)) website, which is operated by the California Institute of Technology, under contract with the National Aeronautics and Space Administration under the Exoplanet Exploration Program. This research made use of Astropy, a community-developed core Python package for astronomy (Astropy Collaboration et al. 2013). This publication makes use of VOSA, developed under the Spanish Virtual Observatory (<https://svo.cab.inta-csic.es>) project funded by MCIN/AEI/10.13039/501100011033/ through grant PID2020-112949GB-I00. VOSA has been partially updated by using funding from the European Union’s Horizon 2020 Research and Innovation Programme under grant agreement No. 776403 (EXOPLANETS-A).

*Facilities:* TESS, Magellan:Clay (Planet Finder Spectrograph), Gemini-South (Zorro), SOAR, LCOGT, MEarth.

*Software:* AstroImageJ (Collins et al. 2017), Astropy (Astropy Collaboration et al. 2013), TAPIR (Jensen 2013), *juliet* (Espinoza et al. 2019), *dynesty* (Speagle 2020).

## Appendix

Here we display the posterior distributions and priors for our joint analysis of the TOI-1075 system. Posterior distributions for the *juliet* joint model parameters are shown in Figure A1. Priors used in the joint analysis are listed in Table A1.

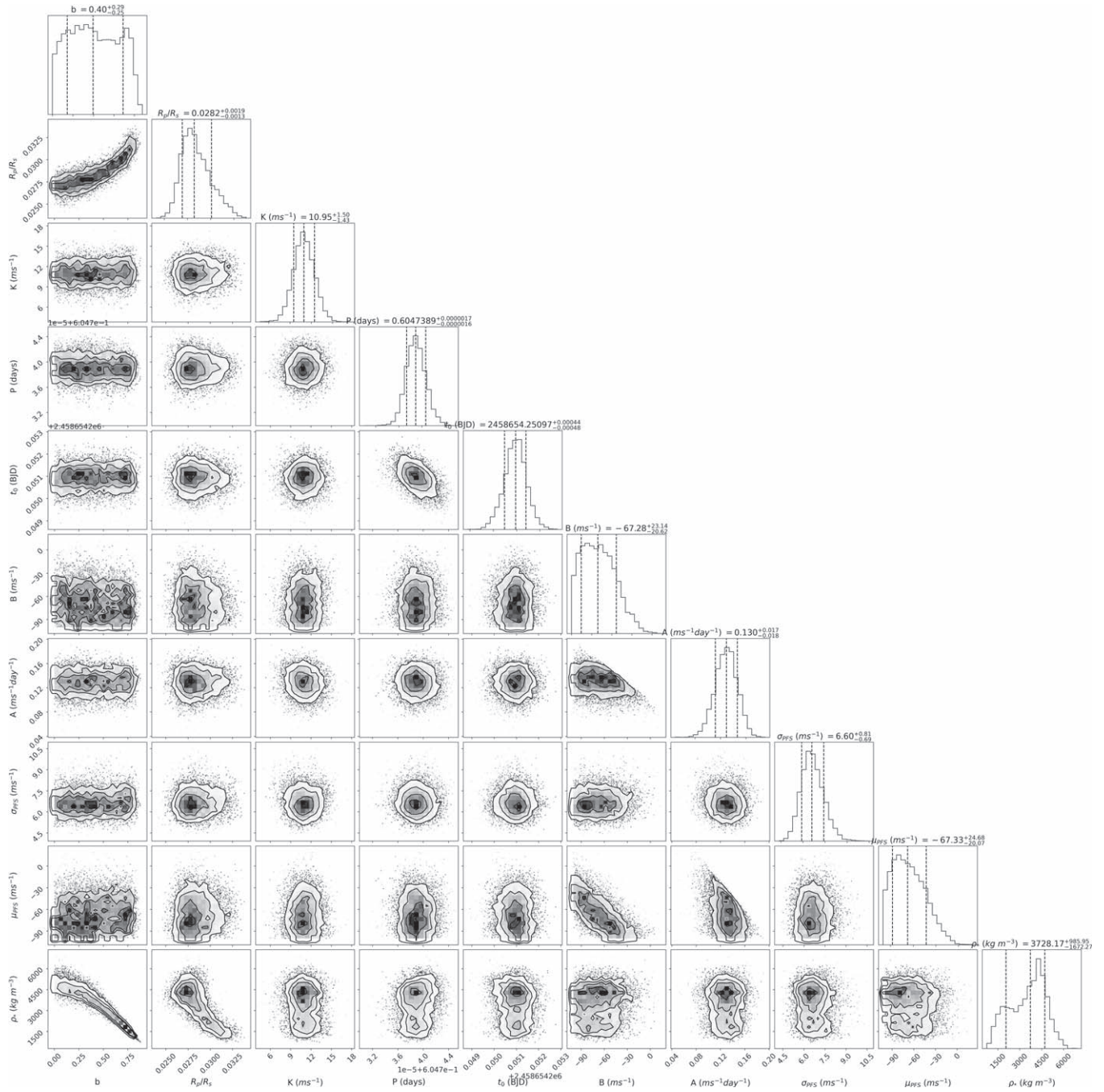


Figure A1. Posterior distribution for the joint (photometric + RV) model parameters derived with juliet.

**Table A1**  
Priors Used in Our Joint Analysis of the TOI-1075 System with *juliet*

Parameter	Prior	Units and Description
<b>Stellar Parameters</b>		
$\rho_*$	$\mathcal{LU}(10^2, 10^5)$	Stellar density of TOI-1075 ( $\text{kg m}^{-3}$ )
<b>Planet Parameters</b>		
$P_b$	$\mathcal{N}(0.6047, 0.0100)$	TOI-1075 b Planet period (days)
$T_{0,b}$	$\mathcal{N}(2,458,654.2500, 0.0100)$	Time of transit center (days)
$r_{1,b}$	$\mathcal{U}(0, 1)$	Parameterization of Espinoza (2018) for $p$ and $b$
$r_{2,b}$	$\mathcal{U}(0, 1)$	Parameterization of Espinoza (2018) for $p$ and $b$
$K_b$	$\mathcal{U}(0, 100)$	RV semiamplitude ( $\text{m s}^{-1}$ )
$e_b$	0.0 (fixed)	Orbital eccentricity
$\omega_b$	90.0 (fixed)	Periastron angle (deg)
<b>Photometry Parameters</b>		
$D_{\text{TESS}}$	1.0 (fixed)	Dilution factor for TESS
$M_{\text{TESS}}$	$\mathcal{N}(0, 0.1)$	Relative flux offset for TESS
$\sigma_{\text{TESS}}$	$\mathcal{LU}(0, 5000)$	Jitter term for TESS light curve (ppm)
$q_{1,\text{TESS}}$	$\mathcal{U}(0, 1)$	Quadratic limb-darkening parameterization (Kipping 2013)
$q_{2,\text{TESS}}$	$\mathcal{U}(0, 1)$	Quadratic limb-darkening parameterization (Kipping 2013)
$D_{\text{LCOGT}}$	1.0 (fixed)	Dilution factor for LCOGT
$M_{\text{LCOGT}}$	$\mathcal{N}(0, 0.1)$	Relative flux offset for LCOGT
$\sigma_{\text{LCOGT}}$	$\mathcal{LU}(0.1, 10^5)$	Jitter term for LCOGT light curve (ppm)
$q_{1,\text{LCOGT}}$	$\mathcal{U}(0, 1)$	Quadratic limb-darkening parameterization (Kipping 2013)
$q_{2,\text{LCOGT}}$	$\mathcal{U}(0, 1)$	Quadratic limb-darkening parameterization (Kipping 2013)
$D_{\text{MEarth}}$	1.0 (fixed)	Dilution factor for MEarth-South
$M_{\text{MEarth}}$	$\mathcal{N}(0, 0.1)$	Relative flux offset for MEarth-South
$\sigma_{\text{MEarth}}$	$\mathcal{LU}(0.1, 10^5)$	Jitter term for MEarth-South light curve (ppm)
$q_{1,\text{MEarth}}$	$\mathcal{U}(0, 1)$	Quadratic limb-darkening parameterization (Kipping 2013)
$q_{2,\text{MEarth}}$	$\mathcal{U}(0, 1)$	Quadratic limb-darkening parameterization (Kipping 2013)
<b>RV Parameters</b>		
$\mu_{\text{PFS}}$	$\mathcal{U}(-100, 100)$	Systemic velocity for PFS ( $\text{m s}^{-1}$ )
$\sigma_{\text{PFS}}$	$\mathcal{LU}(10^{-3}, 100)$	Jitter term for PFS ( $\text{m s}^{-1}$ )
$A$	$\mathcal{U}(-100, 100)$	Slope of linear long-term RV trend ( $\text{m s}^{-1} \text{day}^{-1}$ )
$B$	$\mathcal{U}(-100, 100)$	Intercept of linear long-term RV trend ( $\text{m s}^{-1}$ )

**Note.** The prior labels of  $\mathcal{N}$ ,  $\mathcal{U}$ , and  $\mathcal{LU}$  represent normal, uniform, and log-uniform distributions, respectively, where  $\mathcal{N}(\mu, \sigma^2)$  is a normal distribution of the mean  $\mu$  and variance  $\sigma^2$ , and  $\mathcal{U}(a, b)$  and  $\mathcal{LU}(a, b)$  are uniform and log-uniform distributions between  $a$  and  $b$ .

### ORCID iDs

Zahra Essack  <https://orcid.org/0000-0002-2482-0180>  
 Avi Shporer  <https://orcid.org/0000-0002-1836-3120>  
 Jennifer A. Burt  <https://orcid.org/0000-0002-0040-6815>  
 Sara Seager  <https://orcid.org/0000-0002-6892-6948>  
 Saverio Cambioni  <https://orcid.org/0000-0001-6294-4523>  
 Zifan Lin  <https://orcid.org/0000-0003-0525-9647>  
 Karen A. Collins  <https://orcid.org/0000-0001-6588-9574>  
 Eric E. Mamajek  <https://orcid.org/0000-0003-2008-1488>  
 Keivan G. Stassun  <https://orcid.org/0000-0002-3481-9052>  
 George R. Ricker  <https://orcid.org/0000-0003-2058-6662>  
 Roland Vanderspek  <https://orcid.org/0000-0001-6763-6562>  
 David W. Latham  <https://orcid.org/0000-0001-9911-7388>  
 Joshua N. Winn  <https://orcid.org/0000-0002-4265-047X>  
 Jon M. Jenkins  <https://orcid.org/0000-0002-4715-9460>  
 R. Paul Butler  <https://orcid.org/0000-0003-1305-3761>  
 David Charbonneau  <https://orcid.org/0000-0002-9003-484X>  
 Kevin I. Collins  <https://orcid.org/0000-0003-2781-3207>  
 Jeffrey D. Crane  <https://orcid.org/0000-0002-5226-787X>  
 Tianjun Gan  <https://orcid.org/0000-0002-4503-9705>  
 Coel Hellier  <https://orcid.org/0000-0002-3439-1439>  
 Steve B. Howell  <https://orcid.org/0000-0002-2532-2853>

Andrew W. Mann  <https://orcid.org/0000-0003-3654-1602>  
 Ali Ramadhan  <https://orcid.org/0000-0003-1102-1520>  
 Stephen A. Shectman  <https://orcid.org/0000-0002-8681-6136>  
 Samuel W. Yee  <https://orcid.org/0000-0001-7961-3907>  
 Ismael Mireles  <https://orcid.org/0000-0002-4510-2268>  
 Elisa V. Quintana  <https://orcid.org/0000-0003-1309-2904>  
 Peter Tenenbaum  <https://orcid.org/0000-0002-1949-4720>  
 Guillermo Torres  <https://orcid.org/0000-0002-5286-0251>  
 Elise Furlan  <https://orcid.org/0000-0001-9800-6248>

### References

- Adams, E. R., Jackson, B., & Endl, M. 2016, *AJ*, 152, 47  
 Adams, E. R., Jackson, B., Endl, M., et al. 2017, *AJ*, 153, 82  
 Adams, E. R., Jackson, B., Johnson, S., et al. 2021, *PSJ*, 2, 152  
 Adibekyan, V., Dorn, C., Sousa, S. G., et al. 2021, *Sci*, 374, 330  
 Asphaug, E., & Reufer, A. 2014, *NatGe*, 7, 564  
 Astropy Collaboration, Robitaille, T. P., Tollerud, E. J., et al. 2013, *A&A*, 558, A33  
 Bailer-Jones, C. A. L., Rybizki, J., Fousneau, M., Demleitner, M., & Andrae, R. 2021, *AJ*, 161, 147  
 Batalha, N. E., Lewis, T., Fortney, J. J., et al. 2019, *ApJL*, 885, L25  
 Batalha, N. M. 2014, *PNAS*, 111, 12647  
 Bensby, T., Feltzing, S., & Oey, M. S. 2014, *A&A*, 562, A71

- Benz, W., Anic, A., Horner, J., & Whitby, J. A. 2008, Mercury (Berlin: Springer), 7
- Berta, Z. K., Irwin, J., Charbonneau, D., Burke, C. J., & Falco, E. E. 2012, *AJ*, 144, 145
- Bluhm, P., Luque, R., Espinoza, N., et al. 2020, *A&A*, 639, A132
- Bluhm, P., Pallé, E., Molaverdikhani, K., et al. 2021, *A&A*, 650, A78
- Boro Saikia, S., Marvin, C. J., Jeffers, S. V., et al. 2018, *A&A*, 616, A108
- Borucki, W. J., Koch, D., Basri, G., et al. 2010, *Sci*, 327, 977
- Bourrier, V., Dumusque, X., Dorn, C., et al. 2018, *A&A*, 619, A1
- Boyajian, T. S., von Braun, K., van Belle, G., et al. 2012, *ApJ*, 757, 112
- Brown, T. M., Baliber, N., Bianco, F. B., et al. 2013, *PASP*, 125, 1031
- Bryant, E. M., & Bayliss, D. 2022, *AJ*, 163, 197
- Buchhave, L. A., Dressing, C. D., Dumusque, X., et al. 2016, *AJ*, 152, 160
- Buder, S., Asplund, M., Duong, L., et al. 2018, *MNRAS*, 478, 4513
- Buder, S., Sharma, S., Kos, J., et al. 2021, *MNRAS*, 506, 150
- Butler, R. P., Marcy, G. W., Williams, E., et al. 1996, *PASP*, 108, 500
- Cambioni, S., Asphaug, E., Jung, E., Emsenhuber, A., & Weiss, B. 2022, *LPICo*, 2678, 1979
- Cambioni, S., Jacobson, S. A., Emsenhuber, A., et al. 2021, *PSJ*, 2, 93
- Casagrande, L., Schönrich, R., Asplund, M., et al. 2011, *A&A*, 530, A138
- Chen, H., & Rogers, L. A. 2016, *ApJ*, 831, 180
- Christiansen, J. L., Vanderburg, A., Burt, J., et al. 2017, *AJ*, 154, 122
- Ciardi, D. R., Beichman, C. A., Horch, E. P., & Howell, S. B. 2015, *ApJ*, 805, 16
- Clark, J. T., Wright, D. J., Wittenmyer, R. A., et al. 2022, *MNRAS*, 510, 2041
- Cloutier, R., Charbonneau, D., Stassun, K. G., et al. 2021, *AJ*, 162, 79
- Cloutier, R., & Menou, K. 2020, *AJ*, 159, 211
- Cloutier, R., Rodriguez, J. E., Irwin, J., et al. 2020, *AJ*, 160, 22
- Collins, K. A., Kielkopf, J. F., Stassun, K. G., & Hessman, F. V. 2017, *AJ*, 153, 77
- Crane, J. D., Shectman, S. A., & Butler, R. P. 2006, *Proc. SPIE*, 6269, 626931
- Crane, J. D., Shectman, S. A., Butler, R. P., Thompson, I. B., & Burley, G. S. 2008, *Proc. SPIE*, 7014, 701479
- Crane, J. D., Shectman, S. A., Butler, R. P., et al. 2010, *Proc. SPIE*, 7735, 773553
- Cutri, R. M., Skrutskie, M. F., van Dyk, S., et al. 2003, 2MASS All Sky Catalog of Point Sources
- Cutri, R. M., Wright, E. L., Conrow, T., et al. 2012, *yCat*, II/311
- Dressing, C. D., Charbonneau, D., Dumusque, X., et al. 2015, *ApJ*, 800, 135
- Egeland, R., Soon, W., Baliunas, S., et al. 2017, *ApJ*, 835, 25
- ESA 1997, ESA SP-1200, THE HIPPARCOS and TYCHO Catalogues (Noordwijk: ESA)
- Espinoza, N. 2018, arXiv:1811.04859
- Espinoza, N., Brahm, R., Henning, T., et al. 2020, *MNRAS*, 491, 2982
- Espinoza, N., Kossakowski, D., & Brahm, R. 2019, *MNRAS*, 490, 2262
- Fantini, N. J., Côté, P., McConnachie, A. W., et al. 2019, *ApJ*, 887, 148
- Fuhrmann, K., Chini, R., Kaderhandt, L., & Chen, Z. 2017, *MNRAS*, 464, 2610
- Fulton, B. J., Petigura, E. A., Blunt, S., & Sinukoff, E. 2018, *PASP*, 130, 044504
- Fulton, B. J., Petigura, E. A., Howard, A. W., et al. 2017, *AJ*, 154, 109
- Gaia Collaboration, Brown, A. G. A., Vallenari, A., et al. 2018, *A&A*, 616, A1
- Gaia Collaboration, Smart, R. L., Sarro, L. M., et al. 2021, *A&A*, 649, A6
- Gagné, J., Mamajek, E. E., Malo, L., et al. 2018, *ApJ*, 856, 23
- Giacalone, S., & Dressing, C. D. 2020, triceratops: Candidate exoplanet rating tool, Astrophysics Source Code Library, ascl:2002.004
- Giacalone, S., Dressing, C. D., Hedges, C., et al. 2022, *AJ*, 163, 99
- Giacalone, S., Dressing, C. D., Jensen, E. L., et al. 2021, *AJ*, 161, 24
- Ginzburg, S., Schlichting, H. E., & Sari, R. 2018, *MNRAS*, 476, 759
- Gray, R. O., Corbally, C. J., Garrison, R. F., et al. 2006, *AJ*, 132, 161
- Guenther, E., Barragán, O., Dai, F., et al. 2017, *A&A*, 608, A93
- Guerrero, N. M., Seager, S., Huang, C. X., et al. 2021, *ApJS*, 254, 39
- Gupta, A., & Schlichting, H. E. 2019, *MNRAS*, 487, 24
- Gupta, A., & Schlichting, H. E. 2020, *MNRAS*, 493, 792
- Hébrard, G., Étangs, A., Vidal-Madjar, A., Désert, J.-M., & Ferlet, R. 2003, arXiv:astro-ph/0312384
- Henden, A. A., Templeton, M., Terrell, D., et al. 2016, *yCat*, II/336
- Holzappel, W. B. 2018, *SSSci*, 80, 31
- Howell, S. B., Everett, M. E., Horch, E. P., et al. 2016, *ApJL*, 829, L2
- Howell, S. B., Everett, M. E., Sherry, W., Horch, E., & Ciardi, D. R. 2011, *AJ*, 142, 19
- Howell, S. B., Sobek, C., Haas, M., et al. 2014, *PASP*, 126, 398
- Irwin, J. M., Berta-Thompson, Z. K., Charbonneau, D., et al. 2015, in 18th Cambridge Workshop on Cool Stars, Stellar Systems, and the Sun, Proc. Lowell Observatory, ed. G. van Belle & H. Harris (Flagstaff, AZ: Lowell Observatory), 767
- Ito, Y., & Ikoma, M. 2021, *MNRAS*, 502, 750
- Ito, Y., Ikoma, M., Kawahara, H., et al. 2015, *ApJ*, 801, 144
- Jenkins, J. M. 2002, *ApJ*, 575, 493
- Jenkins, J. M., Chandrasekaran, H., McCauliff, S. D., et al. 2010, *Proc. SPIE*, 7740, 140
- Jenkins, J. M., Twicken, J. D., McCauliff, S., et al. 2016, *Proc. SPIE*, 9913, 99133E
- Jensen, E. 2013, Tapir: A Web Interface for Transit/eclipse Observability, Astrophysics Source Code Library, ascl:1306.007
- Johansen, A., & Dorn, C. 2022, *A&A*, 662, A19
- Johnson, J. A., & Apps, K. 2009, *ApJ*, 699, 933
- Kempton, E. M.-R., Bean, J. L., Louie, D. R., et al. 2018, *PASP*, 130, 114401
- Kervella, P., Arenou, F., & Thévenin, F. 2022, *A&A*, 657, A7
- Kilic, M., Munn, J. A., Harris, H. C., et al. 2017, *ApJ*, 837, 162
- Kipping, D. M. 2013, *MNRAS*, 435, 2152
- Kordopatis, G., Gilmore, G., Steinmetz, M., et al. 2013, *AJ*, 146, 134
- Kostov, V. B., Mullally, S. E., Quintana, E. V., et al. 2019, *AJ*, 157, 124
- Kreidberg, L. 2015, *PASP*, 127, 1161
- Kreidberg, L., Koll, D. D., Morley, C., et al. 2019, *Natur*, 573, 87
- Kruss, M., & Wurm, G. 2018, *ApJ*, 869, 45
- Kunder, A., Kordopatis, G., Steinmetz, M., et al. 2017, *AJ*, 153, 75
- Lallement, R., Capitanio, L., Ruiz-Dern, L., et al. 2018, *A&A*, 616, A132
- Lam, K. W., Csizmadia, S., Astudillo-Defru, N., et al. 2021, *Sci*, 374, 1271
- Lee, E. J., & Chiang, E. 2016, *ApJ*, 817, 90
- Lee, E. J., Chiang, E., & Ormel, C. W. 2014, *ApJ*, 797, 95
- Lee, E. J., & Connors, N. J. 2021, *ApJ*, 908, 32
- Léger, A., Grasset, O., Fegley, B., et al. 2011, *Icar*, 213, 1
- Li, J., Tenenbaum, P., Twicken, J. D., et al. 2019, *PASP*, 131, 024506
- Liu, S.-F., Hori, Y., Lin, D., & Asphaug, E. 2015, *ApJ*, 812, 164
- Lopez, E. D., Fortney, J. J., & Miller, N. 2012, *ApJ*, 761, 59
- Lopez, E. D., & Rice, K. 2018, *MNRAS*, 479, 5303
- Luck, R. E. 2018, *AJ*, 155, 111
- Luque, R., Serrano, L., Molaverdikhani, K., et al. 2021, *A&A*, 645, A41
- Malavolta, L., Mayo, A. W., Louden, T., et al. 2018, *AJ*, 155, 107
- Mamajek, E. E., & Hillenbrand, L. A. 2008, *ApJ*, 687, 1264
- Mann, A. W., Dupuy, T., Kraus, A. L., et al. 2019, *ApJ*, 871, 63
- Mann, A. W., Feiden, G. A., Gaidos, E., Boyajian, T., & von Braun, K. 2015, *ApJ*, 804, 64
- Mansfield, M., Kite, E. S., Hu, R., et al. 2019, *ApJ*, 886, 141
- Marcus, R. A., Sasselov, D., Hernquist, L., & Stewart, S. T. 2010, *ApJL*, 712, L73
- Martinez, C. F., Cunha, K., Ghezzi, L., & Smith, V. V. 2019, *ApJ*, 875, 29
- Maxted, P. F. L., Anderson, D. R., Collier Cameron, A., et al. 2011, *PASP*, 123, 547
- McCully, C., Volgenau, N. H., Harbeck, D.-R., et al. 2018, *Proc. SPIE*, 10707, 107070K
- McQuillan, A., Mazeh, T., & Aigrain, S. 2014, *ApJS*, 211, 24
- Ment, K., Dittmann, J. A., Astudillo-Defru, N., et al. 2019, *AJ*, 157, 32
- Mermilliod, J. C., Mermilliod, M., & Hauck, B. 1997, *A&AS*, 124, 349
- Millholland, S. C., & Spalding, C. 2020, *ApJ*, 905, 71
- Mocquet, A., Grasset, O., & Sotin, C. 2014, *RSPTA*, 372, 20130164
- Morris, R. L., Twicken, J. D., Smith, J. C., et al. 2017, Kepler Data Processing Handbook: Photometric Analysis, Tech. Rep.
- Nardiello, D., Malavolta, L., Desidera, S., et al. 2022, *A&A*, 664, A163
- Noyes, R. W., Hartmann, L. W., Baliunas, S. L., Duncan, D. K., & Vaughan, A. H. 1984, *ApJ*, 279, 763
- Nutzman, P., & Charbonneau, D. 2008, *PASP*, 120, 317
- Osborn, A., Armstrong, D. J., Cale, B., et al. 2021, *MNRAS*, 507, 2782
- Owen, J. E., & Wu, Y. 2017, *ApJ*, 847, 29
- Paegert, M., Stassun, K. G., Collins, K. A., et al. 2021, arXiv:2108.04778
- Pecaut, M. J., & Mamajek, E. E. 2013, *ApJS*, 208, 9
- Pepe, F., Cameron, A. C., Latham, D. W., et al. 2013, *Natur*, 503, 377
- Pollacco, D. L., Skillen, I., Collier Cameron, A., et al. 2006, *PASP*, 118, 1407
- Prusti, T., De Bruijne, J., Brown, A. G., et al. 2016, *A&A*, 595, A1
- Pu, B., & Lai, D. 2019, *MNRAS*, 488, 3568
- Reiners, A., Shulyak, D., Käpylä, P. J., et al. 2022, *A&A*, 662, A41
- Reiners, A., & Zechmeister, M. 2020, *ApJS*, 247, 11
- Ricker, G. R., Winn, J. N., Vanderspek, R., et al. 2014, *JATIS*, 1, 014003
- Rogers, L. A. 2015, *ApJ*, 801, 41
- Rubie, D. C., Jacobson, S. A., Morbidelli, A., et al. 2015, *Icar*, 248, 89
- Santerne, A., Brugger, B., Armstrong, D., et al. 2018, *NatAs*, 2, 393
- Schaefer, L., & Fegley, B. 2009, *ApJL*, 703, L113
- Schlaufman, K. C., & Laughlin, G. 2010, *A&A*, 519, A105
- Schofield, M., Chaplin, W. J., Huber, D., et al. 2019, *ApJS*, 241, 12
- Schröder, C., Reiners, A., & Schmitt, J. H. M. M. 2009, *A&A*, 493, 1099
- Schulze, J., Wang, J., Johnson, J., et al. 2021, *PSJ*, 2, 113

- Scora, J., Valencia, D., Morbidelli, A., & Jacobson, S. 2020, *MNRAS*, **493**, 4910
- Scott, N. J., Howell, S. B., Gnilka, C. L., et al. 2021, *FrASS*, **8**, 138
- Seager, S., Kuchner, M., Hier-Majumder, C., & Militzer, B. 2007, *ApJ*, **669**, 1279
- Serrano, L. M., Gandolfi, D., Mustill, A. J., et al. 2022, *NatAs*, **6**, 736
- Silva, T. A., Demangeon, O., Barros, S., et al. 2022, *A&A*, **657**, A68
- Smith, J. C., Stumpe, M. C., Van Cleve, J. E., et al. 2012, *PASP*, **124**, 1000
- Soto, M. G., & Jenkins, J. S. 2018, *A&A*, **615**, A76
- Sousa, S. G., Adibekyan, V., Delgado-Mena, E., et al. 2018, *A&A*, **620**, A58
- Souto, D., Cunha, K., Smith, V. V., et al. 2022, *ApJ*, **927**, 123
- Speagle, J. S. 2020, *MNRAS*, **493**, 3132
- Stassun, K. G., Collins, K. A., & Gaudi, B. S. 2017, *AJ*, **153**, 136
- Stassun, K. G., Corsaro, E., Pepper, J. A., & Gaudi, B. S. 2018, *AJ*, **155**, 22
- Stassun, K. G., Oelkers, R. J., Paegert, M., et al. 2019, *AJ*, **158**, 138
- Stassun, K. G., Oelkers, R. J., Pepper, J., et al. 2018, *AJ*, **156**, 102
- Stassun, K. G., & Torres, G. 2016, *AJ*, **152**, 180
- Stassun, K. G., & Torres, G. 2021, *ApJL*, **907**, L33
- Steinmetz, M., Matijević, G., Enke, H., et al. 2020, *AJ*, **160**, 82
- Stumpe, M. C., Smith, J. C., Catanzarite, J. H., et al. 2014, *PASP*, **126**, 100
- Stumpe, M. C., Smith, J. C., Van Cleve, J. E., et al. 2012, *PASP*, **124**, 985
- Tononi, J., Torres, S., García-Berro, E., et al. 2019, *A&A*, **628**, A52
- Trotta, R. 2008, *ConPh*, **49**, 71
- Twicken, J. D., Catanzarite, J. H., Clarke, B. D., et al. 2018, *PASP*, **130**, 064502
- Twicken, J. D., Clarke, B. D., Bryson, S. T., et al. 2010, *Proc. SPIE*, **7740**, 774023
- Ugoren, A. R., Grossenbacher, R., Penhallow, W. S., MacConnell, D. J., & Frye, R. L. 1972, *AJ*, **77**, 486
- Van Eylen, V., Agentoft, C., Lundkvist, M., et al. 2018, *MNRAS*, **479**, 4786
- Veyette, M. J., Muirhead, P. S., Mann, A. W., et al. 2017, *ApJ*, **851**, 26
- Weidenschilling, S. 1978, *Icar*, **35**, 99
- Yee, S. W., Petigura, E. A., & von Braun, K. 2017, *ApJ*, **836**, 77
- Zeng, L., Jacobsen, S. B., Hyung, E., et al. 2021, *ApJ*, **923**, 247
- Zeng, L., Jacobsen, S. B., & Sasselov, D. D. 2017, *RNAAS*, **1**, 32